PAPER

Check for updates

MXene-derived potassium titanate nanoribbon-decorated electrode architecture for the detection of ciprofloxacin: development of a multipurpose sensing platform promoting One Health

Arghya Chakravorty, †[a] Sudip Das, †[a] Aarcha Appu Mini,†[a] Shikha Awasthi, [b] Sarvesh Kumar Pandey*[c] and Vimala Raghavan *[a]

Recent studies have highlighted the promise of MXene-derived titanate nanoribbons (KTNR) as electrode materials for electrochemical sensing applications. This work investigates the electrochemical activity of potassium titanate nanoribbons synthesized from MXene for the development of a voltammetric sensor for ciprofloxacin detection. The sensor offers a sustainable approach for ciprofloxacin quantification, addressing critical needs in food safety, environmental monitoring, and healthcare diagnostics, ultimately contributing to the United Nations' Sustainable Development Goals by mitigating antimicrobial resistance and supporting the One Health initiative. To initiate the experiments, the structural, stability/energetics, and electronic features of two dimer complexes, KTNR/ciprofloxacin and MXene/ciprofloxacin, had been computationally inspected using two *in silico* tools, and some important electronic parameters such as binding energy, HOMO–LUMO gap and dipole moment showed that the former one (KTNRs) was significantly more sensitive than the MXene with ciprofloxacin. 2D Ti_3C_2 MXene served as the precursor for the synthesis of potassium titanate nanoribbons. X-ray diffraction (XRD), field emission scanning electron microscopy (FESEM), high-resolution transmission electron microscopy (HRTEM), selected area electron diffraction (SAED), elemental mapping, and energy-dispersive X-ray spectroscopy (EDX) techniques were employed to confirm the crystallinity, surface morphology, and layered structure of the synthesized nanoribbons. Atomic force microscopy (AFM), contact angle measurement and surface profilometry were used to characterize the fabricated electrode surface. The electrochemical and sensing properties of the materials were further evaluated using cyclic voltammetry (CV), differential pulse voltammetry (DPV), and electrochemical impedance spectroscopy (EIS). Subsequently, the nanoribbons were deposited onto a glassy carbon electrode (GCE) surface. The electro-oxidation behaviour of ciprofloxacin was then investigated using CV, DPV, and square wave voltammetry (SWV) in an optimized 0.1 M phosphate buffer solution (pH 8). The developed sensor exhibited a remarkable linear detection range of 0.6 μM (≈ 0.03 μg mL^{-1}) to 147.2 μM (≈ 7.18 μg mL^{-1}) for ciprofloxacin. Additionally, the limit of detection (LOD) achieved was 0.07, 0.0608, and 0.0264 μM for CV, DPV, and SWV, respectively. Notably, the electrodes demonstrated excellent selectivity towards ciprofloxacin detection in complex matrices, including marine water, river water, agricultural soil, organic fertilizer, milk, honey, poultry eggs, and simulated body fluids.
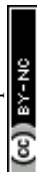
[a] *Centre for Nanotechnology Research, Vellore Institute of Technology, Vellore, Tamil Nadu, 632014, India. E-mail: vimala.r@vit.ac.in*

[b] *Department of Basic Sciences, IES University Bhopal, Bhopal, Madhya Pradesh, 462044, India*

[c] *Department of Chemistry, Maulana Azad National Institute of Technology Bhopal, Bhopal, Madhya Pradesh, 462 003, India. E-mail: sarvesh@manit.ac.in*

† These authors contributed equally to this manuscript.

1. Introduction

Ciprofloxacin is a double-edged sword. While it is a crucial antibiotic, its overuse and presence in the environment and food contribute significantly to the global antimicrobial resistance (AMR) crisis. It is an antibiotic with the ability to inhibit bacterial DNA gyrase. It is used to treat humans with a variety of bacterial infections, including urinary tract infections, respiratory tract infections, skin infections, and certain sexually transmitted diseases.

It is also evident, that like the other broad-spectrum fluoroquinolone group of antibiotics, ciprofloxacin is also predominantly effective in growth promotion and treating several deadly infections in animal husbandry, including cattle farms, poultry farms, fisheries, and apiculture. However, overuse and misuse of antibiotics like ciprofloxacin are responsible for the development of (AMR). The relationship between AMR and ciprofloxacin lies in the selective pressure exerted by the widespread use of this antibiotic. When bacteria are exposed to ciprofloxacin, some of them may possess genetic mutations or acquire resistance genes that enable them to survive the antibiotic's effects. Through natural selection, these resistant bacteria can then proliferate and spread, leading to the emergence of ciprofloxacin-resistant strains. Ciprofloxacin-resistant bacteria pose a significant challenge. Infections caused by them become more difficult to treat, requiring stronger antibiotics, alternative therapies, and precision dosing through therapeutic drug monitoring. This can lead to longer hospital stays, increased healthcare costs, and even higher mortality rates.[1–9]

The WHO reports show variations, but ciprofloxacin resistance in bacteria like *E. coli* and *Klebsiella pneumoniae* can range from 4% to 93% across countries.[10] This highlights the growing global problem. Traces of ciprofloxacin can end up in rivers and marine environments through wastewater. Studies suggest that even low concentrations of ciprofloxacin in the environment can promote AMR in *E. coli* present there. In brief, it can affect the whole marine and freshwater ecosystem. Through the food chain, the resistant bacteria and the antibiotic residues enter the human system, and even animal-based foods like eggs, meat, milk, and honey also contain ciprofloxacin residues. This further significantly complicates the same global challenges.[11–16]

As a diagnostic analytical approach to measuring the concentration of different bio-analytes[17–20] and antibiotics,[21–25] specifically ciprofloxacin, several versatile and efficient analytical tools have been developed like ultra-high performance liquid chromatography-mass spectrometry, quadrupole time of flight mass-spectroscopy, and liquid chromatography-mass spectrometry, which are recognized as a gold standard tool to measure ciprofloxacin concentration in food (*viz.* milk, eggs, meat, fish, honey), environmental (wastewater, river and marine water, agricultural soils, organic fertilizers), and biomedical (*viz.* body fluids like blood serum, urine) samples.[26] Though these tools are highly reliable, sensitive, and efficient in measuring a wide concentration range, due to the high expenditure and maintenance these techniques are unable to be installed in resource-limited settings. In this context, the development of alternative versatile technologies is highly required to measure ciprofloxacin concentration in various real matrices. Thus, a cost-effective electrode material has been reported (as shown in Scheme 1) by using MXene-derived potassium titanate nanoribbons. Here, the electro-catalysis of ciprofloxacin has been demonstrated as a fundamental mechanistic approach.

In our study, we have already explored the potential of novel nanoribbons derived from MXene (titanium carbide) as an electrochemical sensing platform to provide food safety. These nanoribbons like 2D MXene[27] possess several unique characteristics that make them ideal for this application. Firstly, they possess an intrinsic ability to amplify signals within the material itself, eliminating the need for separate amplifiers. They exhibit exceptional stability over time, ensuring reliable performance, and demonstrate high sensitivity toward analytes crucial for food safety, as reported by Mini and Raghavan (2024).[28] The specific structure of these nanoribbons, with their layered morphology and abundant hydroxyl groups on the surface, provides a large surface area, making them well-suited for ciprofloxacin detection. In addition to that, the presence of polar bonds in ciprofloxacin is due to the electronegativity
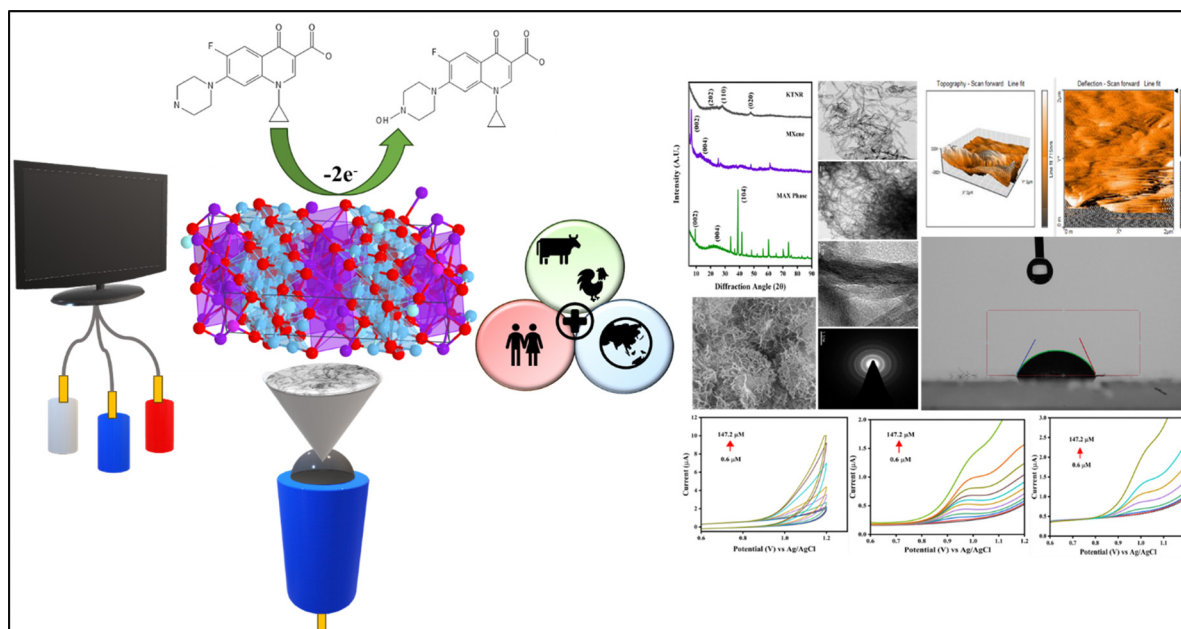
Scheme 1 Schematic illustration of the KTNR fabricated multi-purpose electrochemical sensor for ciprofloxacin detection.

difference between the atoms involved in its chemical structure. Here, the presence of polar bonds leads to an uneven distribution of electron density within the molecule, resulting in regions of partial positive and partial negative charge. This polarity allows ciprofloxacin to interact with other polar molecules or ions, which is important for its mechanism of action as an antibiotic and for its solubility in aqueous environments, as well as facilitating its electrocatalytic behaviour.[1–3,28–36] Interestingly, our research shows that ciprofloxacin, a molecule with polarity, triggers a decrease in the resistance of these nanoribbons during the catalytic events. This finding contributes to a deeper understanding of electrochemical sensing mechanisms that exploit proton conduction. Our work highlights the promise of this electrocatalytic approach for achieving ultra-low limits of ciprofloxacin detection with exceptional selectivity even in different real and complex matrices. These are again related to ciprofloxacin sensing for food and environmental safety along with biomedical purposes like therapeutic drug monitoring (TDM).

2. Experimental section

2.1. Computational methodology

Computational tools have an imperative role in understanding and unraveling the quantum (atomic and molecular) level features. Due to the large size of both dimer complexes (KTNR-ciprofloxacin and MXene-ciprofloxacin) consisting of a large number of heavy metals (like K and Ti in the KTNR and Ti in the MXene), the calculations demanded high computational costs. The optimization and frequency calculations have been executed using the semiempirical approach; however, an *ab initio*, Hartree–Fock (HF) functional and 6-31G basis set have been used for single point calculations for the F, O, N, C, N, H, and K atoms and SDD for the Ti (transition metal) atom. Thus, by keeping the experimental facets, this report discusses some important geometry, energetic/stability, and electronic parameters using molecular modelling and electronic feature analyses in the framework of semiempirical and *ab initio* modeling approaches. All quantum chemical calculations have been executed using the immensely used Gaussian 09 electronic structure calculations package.[37]

2.2. Reagents and equipment

Ciprofloxacin ($\geq$99.0%; pharmaceutical secondary standard), enrofloxacin ($\geq$99.0%), norfloxacin ($\geq$98%, TLC), ofloxacin ($\geq$98%; Pharmaceutical Secondary Standard), Nafion, uric acid ($\geq$99%, crystalline), urea (99.0–100.5%, ACS reagent), dopamine hydrochloride ($\geq$98%; Pharmaceutical Secondary Standard), diclofenac sodium ($\geq$98%; Pharmaceutical Secondary Standard), D-glucose ($\geq$99.5% – GC, BioXtra), 48% hydrofluoric acid ($\geq$99.99% trace metals basis), titanium aluminium carbide MAX phase (910 775; $\geq$90%, $\leq$40 μm particle size), and ascorbic acid ($\geq$98%; Pharmaceutical Secondary Standard) were purchased from Sigma Aldrich, India. Other supporting reagents were procured from SD Fine Chemicals, Mumbai, India; Avra Synthesis Pvt. Ltd, India. All the chemicals were used without any further purification. 0.1 M NaH_2PO_4 and 0.1 M Na_2HPO_4 were used to prepare a phosphate buffer solution with the required pH.

Powder X-ray diffraction (XRD) (Bruker D8 Advance, Panalytical X Pert3, Germany, Netherlands), field emission scanning electron microscopy (FE-SEM), and energy-dispersive X-ray analysis (EDAX) (Thermo Fisher, FEI QUANTA 250 FEG), high-resolution transmission electron microscope (HR-TEM) and selected area electron diffraction (SAED) (FEI – TECNAI, G2-20 TWIN – Operating voltage 200 kV) have been used to characterize materials and provided the high-resolution images of the internal structures of the active electrode material, including details of its crystal lattice, atomic arrangements, and defects down to the atomic level. The CHI 660C electrochemical workstation has been used for all electrochemical measurements including cyclic voltammetry (CV), differential pulse voltammetry (DPV), square wave voltammetry (SWV), and electrochemical impedance spectroscopy (EIS). The fabricated electrode surfaces were characterized by an atomic force microscope (Nanosurf AFM, Nanosurf, Switzerland), surface profilometer (Marsurf XR20, Mahr), and wettability test (contact angle metre HO-IAD-CAM-01A, HOLMARC). Throughout the experiments, 0.3 μm alumina slurry was used to polish the active surface of a glassy carbon electrode (GCE) for use as a working electrode, while Ag/AgCl (3 M KCl) and platinum wire performed as a reference and counter electrode in a three-electrode system.

2.3. Synthesis of MXene and MXene-derived potassium titanate nanoribbons (KTNRs)

MXene was synthesized by the priorly optimized HF etching of the MAX phase and delaminated by DMSO.[38,39] Potassium titanate nanoribbons (KTNRs) were synthesized *via* a well-established methodology employing MXene as the precursor.[40] In the initial stage, 100 mg of MXene was incorporated into a mixture composed of 30 mL of 1 M KOH solution and 0.68 mL of 30% H_2O_2. This resultant mixture was subsequently transferred to a 50 mL Teflon-lined stainless-steel autoclave. The autoclave underwent hydrothermal treatment at 150 °C for a duration of 16 hours, facilitating the transformation of MXene into KTNRs. Following natural cooling of the autoclave to ambient temperature, the uppermost layer, containing a white suspension, was isolated using vacuum filtration. The obtained KTNR sample was then subjected to rigorous washing with deionized (DI) water and ethanol to eliminate any residual byproducts from the reaction. Finally, the purified KTNRs were desiccated in an oven at 60 °C for 12 hours to remove any remaining solvent molecules.[28,41,42]

2.4. Preparation of complex matrices

The performance of the fabricated KTNR electrochemical sensor was evaluated in various real-world matrices with clinical significance for trace ciprofloxacin detection. These matrices included simulated body fluid (SBF) to mimic physiological conditions and animal-derived food samples (honey, milk, and eggs) obtained from local markets in Kerala and Tamil Nadu, India. Environmental water samples were also tested, encompassing river water (Ganga) and marine water (Bay of Bengal) collected from West Bengal, India. Additionally, agricultural

soil and organic fertilizer were analyzed, and sourced from local agricultural fields and farms in Vellore, India.

A standardized sample preparation procedure was employed for food and environmental samples. Briefly, samples were homogenized and filtered using a 0.22 μm nylon filter. Subsequently, they underwent a 10-fold dilution with phosphate buffer (pH 8) before being spiked with ciprofloxacin to achieve a concentration (including 15 μM). For agricultural samples, 1 g of the solid material was ultrasonicated in 10 mL of deionized (DI) water, followed by centrifugation at 3000 rpm for 10 minutes. The resulting supernatant was collected, filtered with a 0.22 μm nylon filter, diluted 10-fold with phosphate buffer (pH 8), and spiked with ciprofloxacin to reach a final concentration of 15 μM.

3. Results and discussion

3.1. Computational studies

Comprehensive computational studies on the structural, stability/energetic, and electronic features of a variety of molecular systems can be viewed in the reports along with biomaterials.[43,44] All optimized structures (monomer constituents and dimer complexes) are shown in Fig. 1. Here in this report, a few chosen structural/geometrical parameters (particularly, the bond distance between the atoms of two interacting monomer constituents) have been calculated for both dimer complexes (KTNR/ciprofloxacin and MXene/ciprofloxacin) which are shown in Fig. 1. Having a look into the first case as the KTNR/ciprofloxacin dimer complex, a total of five nonbonding interactions between two components (KTNR and ciprofloxacin) were shown in the dotted line. The bond lengths of the two K···N (3.040 Å and 2.919 Å) and three weak C–H···O (2.120 Å, 2.162 Å, and 2.489 Å) H-bonding

interactions involved in the KTNR/ciprofloxacin dimer complex can be seen in Fig. 1. However, only two metal–nonmetal interactions (Ti···O) could be discerned for the MXene-ciprofloxacin dimer complex whose bond lengths are 2.029 Å and 2.189 Å. The structural parameters appeared to indicate that the former one (KTNR/ciprofloxacin) could be structurally more favorable than the latter one (MXene/ciprofloxacin).

In order to inspect the sensitivity/binding feature (also, linked to the structural features) of both dimer complexes (KTNR-ciprofloxacin and MXene-ciprofloxacin), the binding energies (BEs) were analyzed, which can be seen in Table 1.[45] The semiempirical approach (PM6) showed that the BE of the KTNR-ciprofloxacin complex (254.6 kcal mol^{-1}) was found to be five times greater than that of the MXene-ciprofloxacin complex (-50.6 kcal mol^{-1}). Very importantly and notably, the HF/6-31G method also showed that the BE of the former one (-501.8 kcal mol^{-1}) was found to be 5.4 times stronger than that of the latter one (-92.7 kcal mol^{-1}). Such BE-based findings clearly demonstrated that the KTNRs were more sensitive than the MXene with ciprofloxacin, which also supports the experiment-based outcomes in the later part of the research.

Moreover, as the Frontier molecular orbitals (FMOs), like highest occupied molecular (HOMO) and lowest unoccupied molecular orbital (LUMO), and the associated HOMO–LUMO energy gap (E_{Gap}) are useful diagnostics of showing the sensitivity/reactivity features, such parameters (HOMO, LUMO, and E_{Gap}) were probed. A system having low E_{Gap} value showed that the system was more sensitive/chemically reactive. The E_{Gap} of both the KTNR-ciprofloxacin and MXene-ciprofloxacin complexes was detected as 4.87 eV and 5.568 eV, respectively, which further validated that the former one was more sensitive than the latter one. Interestingly, a system consisting of a large
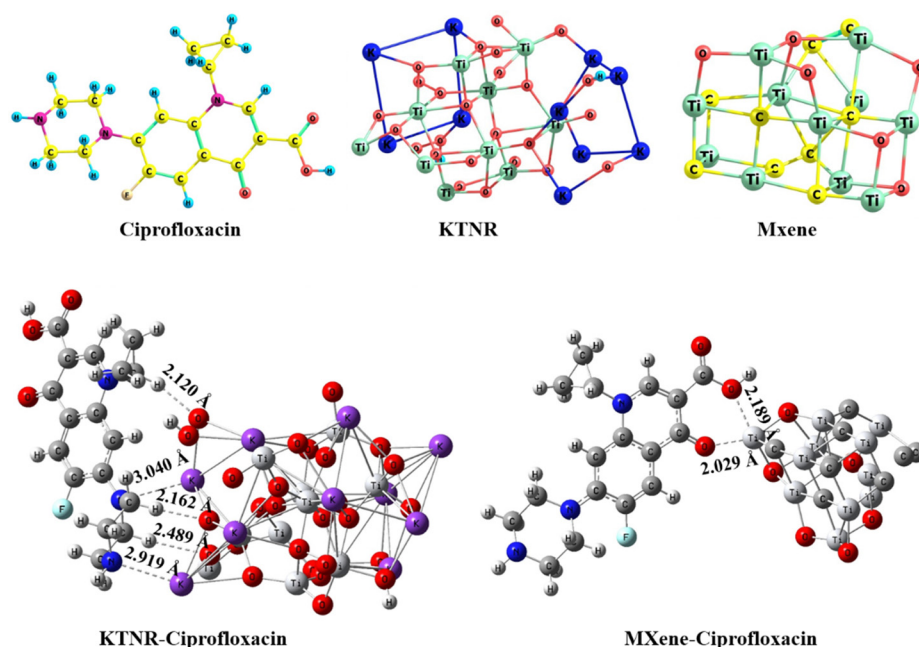

Fig. 1 Optimized structures of the monomer constituents (ciprofloxacin, KTNR, and MXene) and dimer complexes (KTNR–ciprofloxacin and MXene-ciprofloxacin).
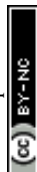
Table 1 Some important and chosen electronic parameters of the KTNR-ciprofloxacin and MXene-ciprofloxacin dimer complexes

System	KTNR-ciprofloxacin	MXene-ciprofloxacin
BE (PM6)	-254.6 kcal mol^{-1}	-50.6 kcal mol^{-1}
BE [HF (SP)/6-31G]	-501.8 kcal mol^{-1}	-92.7 kcal mol^{-1}
HOMO	-5.480	-5.818
LUMO	-0.610	0.250
E_{Gap}	4.87	5.568
Dipole moment	32.1	23.8
Natural charge (e)	KTNR ($0.023e$) and ciprofloxacin ($-0.023e$)	MXene ($0.415e$) and ciprofloxacin ($-0.415e$)

dipole moment (DM) indicated it's more sensitivity/chemical reactivity. Here, in this report the DMs of the KTNR- and MXene-based complexes were computed as 32.1 Debye (D) and 23.8 D which also assured the more sensitivity of the former one. Additionally, the natural charges on each monomer constituent of both dimer complexes were examined and it was found that the ciprofloxacin consisted of negative charge ($-0.023e$) and KTNRs had a positive charge ($+0.023e$). A similar trend can be viewed in the case of the MXene-ciprofloxacin complex where a significant large charge difference (MXene: $+0.415e$ and ciprofloxacin: $-0.415e$) was found therein. Such findings illustrate that the charge transfer (CT) took place from KTNR/MXene to the ciprofloxacin component.

Finally, the FMOs such as HOMO, LUMO, and single-occupied molecular orbital (SOMO) have had a significant role in the electronic transition phenomenon.[46] The HOMO of the KTNR-ciprofloxacin complex was distributed over only some of the Ti-metals of the KTNR component whereas importantly, a SOMO appeared to be located near a single K-metal atom. Very interestingly, the HOMO of the MXene-ciprofloxacin was spread over the some of the Ti–C bonds while the LUMOs were

revealed to be distributed over the C-atoms of two benzene rings, which demonstrated a π to π* transition.

3.2. XRD analysis

The XRD pattern in the image is consistent with the conversion of Ti$_3$AlC$_2$ MAX phase to Ti$_3$C$_2$T$_x$ MXene followed by conversion to KTNRs (Fig. 3(A)). The presence of a high-intensity peak of the precursor Ti$_3$AlC$_2$ MAX phase at an angle of $2\theta = 38.9°$ at (104) signifies elemental Al. After being etched with HF, the layers become more separated and the (104) peak disappears, which denotes the removal of Al. The diffraction peaks at (002), and (004) were assigned for Ti$_3$C$_2$T$_x$ MXene. This increases the d-spacing of the (002) peak, which can be observed as a shift of the peak to a lower angle in the XRD pattern.[47] The successful synthesis of delaminated MXene was followed by the hydrothermal synthesis of KTNRs.

To comprehend the structure in detail, K$_2$Ti$_4$O$_9$ crystallizes in the monoclinic $C2/m$ space group.[48] There are two inequivalent K^{1+} sites. In the first K^{1+} site, K^{1+} is bonded in an 8-coordinate geometry to eight O^{2-} atoms. There is a spread of K–O bond distances ranging from 2.78–3.01 Å. In the second
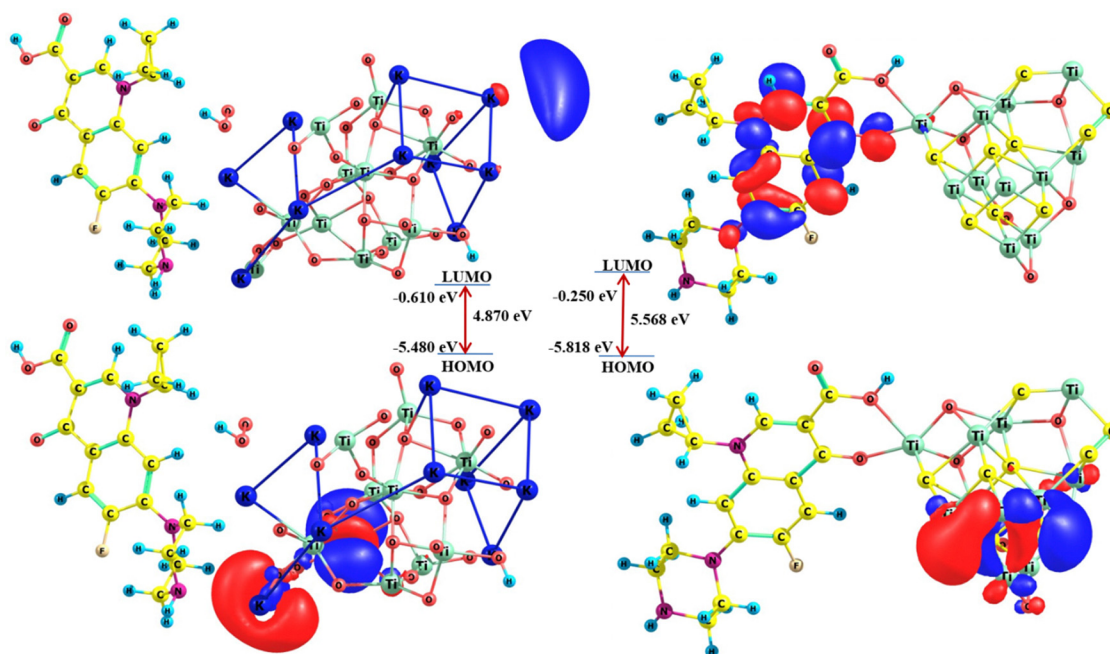

Fig. 2 The three-dimensional (3D) HOMO–LUMO isosurface maps of the dimer complexes (left: KTNR-ciprofloxacin and right: MXene-ciprofloxacin) (bottom: HOMO and top: LUMO).

K^{1+} site, K^{1+} is bonded in a 6-coordinate geometry to six O^{2-} atoms. There is a spread of K–O bond distances ranging from 2.68–3.08 Å. There are four inequivalent Ti^{4+} sites. In the first Ti^{4+} site, Ti^{4+} is bonded in a 6-coordinate geometry to six O^{2-} atoms. There are a spread of Ti–O bond distances ranging from 1.76–2.27 Å. In the second Ti^{4+} site, Ti^{4+} is bonded to six O^{2-} atoms to form a mixture of distorted corner and edge-sharing TiO_6 octahedra. The corner-sharing octahedral tilt angles are 32°. There is a spread of Ti–O bond distances ranging from 1.77–2.22 Å. In the third Ti^{4+} site, Ti^{4+} is bonded in a 6-coordinate geometry to six O^{2-} atoms. There is a spread of Ti–O bond distances ranging from 1.73–2.35 Å. In the fourth Ti^{4+} site, Ti^{4+} is bonded to six O^{2-} atoms to form a mixture of distorted corner and edge-sharing TiO_6 octahedra. The corner-sharing octahedral tilt angles are 30°. There is a spread of Ti–O bond distances ranging from 1.79–2.19 Å. There are nine inequivalent O^{2-} sites. In the first O^{2-} site, O^{2-} is bonded in a distorted rectangular see-saw-like geometry to two equivalent K^{1+} and two Ti^{4+} atoms. In the second O^{2-} site, O^{2-} is bonded

in a distorted single-bond geometry to six K^{1+} and one Ti^{4+} atom. In the third O^{2-} site, O^{2-} is bonded to two equivalent K^{1+} and two Ti^{4+} atoms to form distorted OK_2Ti_2 tetrahedra that share corners with two equivalent OK_2Ti_2 tetrahedra, corners with five OTi_4 trigonal pyramids, and an edge–edge with one OTi_4 trigonal pyramid. In the fourth O^{2-} site, O^{2-} is bonded in a distorted rectangular see-saw-like geometry to two equivalent K^{1+} and two Ti^{4+} atoms. In the fifth O^{2-} site, O^{2-} is bonded in a distorted linear geometry to two equivalent K^{1+} and two Ti^{4+} atoms. In the sixth O^{2-} site, O^{2-} is bonded in a 4-coordinate geometry to four Ti^{4+} atoms. In the seventh O^{2-} site, O^{2-} is bonded to four Ti^{4+} atoms to form distorted OTi_4 trigonal pyramids that share corners with three equivalents OK_2Ti_2 tetrahedra, corners with three OTi_4 trigonal pyramids, and edges with two equivalent OTi_4 trigonal pyramids. In the eighth O^{2-} site, O^{2-} is bonded in a 3-coordinate geometry to three Ti^{4+} atoms. In the ninth O^{2-} site, O^{2-} is bonded to four Ti^{4+} atoms to form distorted OTi_4 trigonal pyramids that share corners with two equivalents OK_2Ti_2 tetrahedra, corners with three OTi_4
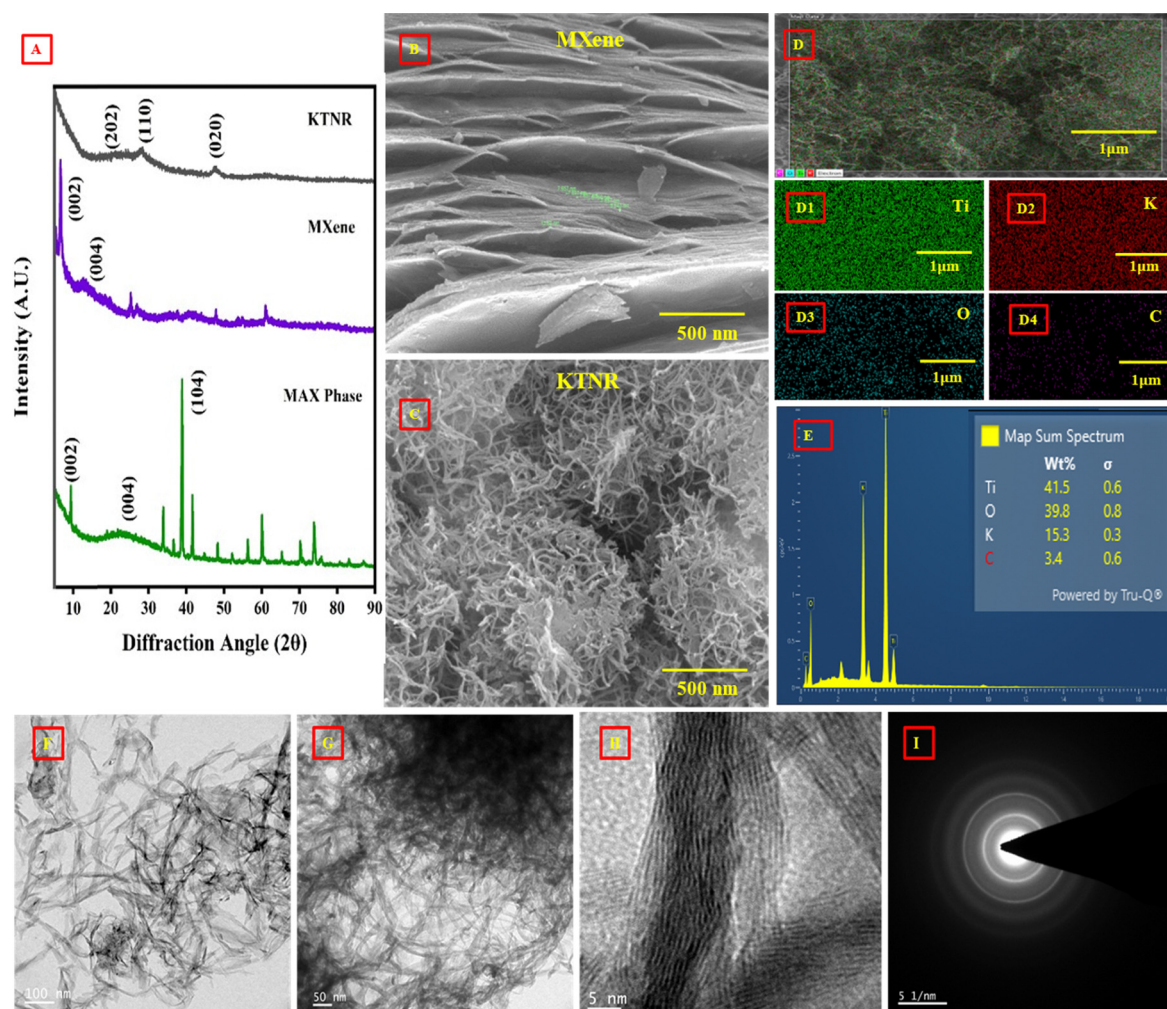

Fig. 3 (A) XRD analysis of the KTNR, MXene and, MAX phase in the range of (2θ) 5–90°; FE-SEM images of (B) MXene, and (C) KTNRs; elemental mapping of (D) all elemental compositions together in the KTNRs; atomic distribution of (D1) titanium, (D2) potassium, (D3) oxygen, and (D4) carbon in a selected section of the matrix of the KTNRs; (E) EDAX spectrum of elements of K:Ti:O:C; HR-TEM of the KTNRs at (F) 100 nm, (G) 50 nm and, (H) 5 nm scales showing different lattices including the multiring SAED pattern (I) to confirm its polycrystallinity.

trigonal pyramids, an edge–edge with one OK_2Ti_2 tetrahedra, and edges with four OTi_4 trigonal pyramids.

The XRD also suggested a monoclinic phase indexing having a Bravais lattice space group $C2/m$. The unit cell had parameters a = 18.25 Å, b = 3.791 Å, c = 12.01 Å, β = 106.4 Å, and volume Å^3. The diffraction angles with corresponding $h\,k\,l$ values and d-spacing were calculated as (2 0 2), 2θ = 20.696, d = 4.2882 nm; (1 1 0), 2θ = 23.997, d = 3.705 nm; (0 2 0), 2θ = 47.953, d = 1.8955 nm. There are also some unidentified peaks present in the XRD pattern, which could be due to impurities or minor phases in the sample. It was evident that MXene had been successfully converted to KTNRs after undergoing oxidation and alkalization[29] considering that the measured peak positions and intensities are consistent with those of JCPDS No. 32-0861 for $K_2Ti_4O_9$ (KTNRs).

3.3. FESEM, EDAX, and mapping analysis

The surface morphology of the materials was confirmed using FESEM performed for $Ti_3C_2T_x$ MXene which clearly showed stacking between the multi-layered structure (Fig. 3(B)).[49] The width of ultrafine layers corresponded to a range varying from 6.76 nm to 12.62 nm. The inter-spacing between the layers ranged from 20 nm to 550. The FESEM images of the KTNRs depicted a distinct webbed-like complex network of nanoribbons having high surface area and porosity (Fig. 3(C)). The width/diameter of the nanoribbons ranged from 9.7 nm to 16.4 nm indicating the uniform morphology. Furthermore, the EDAX and mapping were done to obtain the atomic weight distribution (wt%) of K, Ti, and O relating to 41.5%, 39.8% and 15.3%, respectively, throughout the matrix correlating to the successful synthesis of KTNRs. The uniform abundance of all procured elements K, Ti, and O (Fig. 3(D and E)) makes it a perfect candidate to achieve enhanced electrocatalytic activity of the nanocomposite, especially due to the notable presence of bimetallic potassium and titanium in the matrix. The presence of carbon (3.4 wt%) as recorded in EDAX was observed probably due to some incomplete alkalization of the precursor MXene.

3.4. HRTEM and SAED pattern analysis

HRTEM images further revealed the structural evolution from MXene nanosheets to KTNR nanoribbons. Due to the simultaneous oxidation and alkalization processes, the KTNRs were assumed to have a diameter of around 10 nm (Fig. 3(F–H)). As shown in Figure, HRTEM images validated the ultrafine widths as low as $\sim$2.3 nm and ultrathin thickness of $\sim$1.6 nm, while the lattice spacings averaged at 0.745 nm. The width or thickness is comparatively less than that of the precursor Ti_3C_2 MXene, thereby demonstrating the advantages of the morphological advancement in the nano-scale. Also, the HR-TEM results suggest that the KTNR exists in single or few layers, which is practically impossible to achieve in MXene. In a polycrystalline material having monoclinic phase, the electrons will diffract at a range of angles, producing rings on the SAED pattern. KTNR also showed a multiring SAED pattern that confirmed the polycrystalline nanostructures with distinct phases (Fig. 2(I)).

3.5. Surface optical profilometry, AFM, and contact angles

Fig. 4(A1 and A2) show a line profile obtained from surface profilometry, likely representing the height variations along a specific line on the GCE surface. The provided data likely corresponded to specific roughness parameters measured by the profilometer. The roughness of the surface can influence the performance of the electrode in electrochemical applications. A moderately rough surface can provide more active sites for reactions compared to a flat surface. The both MXene (41 319.6231 nm) and KTNR (41 249.6805 nm) showed similar R values, indicating comparable overall roughness across the measured profiles. MXene (44 811.3649 nm) has a higher M value compared to KTNR (43 641.228 um). A higher M value signifies more prominent height variations throughout the profile. Both materials likely introduce roughness, potentially increasing the surface area for improved sensor performance. MXene might have had a surface with sharper peaks and valleys compared to the KTNRs, based on the higher M value. The width values (around 0.89 μm for both) might represent the width measured at a specific height threshold and may not reflect the actual width of the MXene sheets or the average width of the KTNR nanoribbons. The position values (around 1.56 μm for both) corresponded to the location where the ASH (average surface height) was measured. MXene (3491.74 nm) has a higher ASH compared to the KTNRs (2391.91 nm). This suggested that the MXene layer sits higher on average relative to the reference plane compared to the potassium titanate nanoribbons. Increased surface roughness and higher ASH could be beneficial for electrochemical sensors by providing more sites for analyte molecules to adsorb. This could potentially improve the sensitivity of the sensor. However, the optimal surface characteristics depend on the specific target analyte and the desired electrochemical process. Both MXene and KTNR appeared to introduce roughness to the GCE surface, which could be advantageous for sensor applications. MXene might offer a slightly higher surface area due to its roughness characteristics and higher average surface height. However, further analysis and testing are necessary to determine how these surface properties translate to sensor performance for specific target molecules. However, excessively rough surfaces can hinder electron transfer kinetics.

To consider AFM, both MXene and the KTNRs had an image size of 2 μm, indicating the area scanned by the AFM tip (Fig. 4(B1 and B2)). This allowed for a direct comparison of the surface features within this defined area. The area (4.031 pm^2) was identical for both samples as it represents the total analysed surface area by the AFM, which was likely the same for both measurements. The surface topography parameters *i.e.*, Sa (surface area) for MXene (73.43 nm) had a significantly higher Sa compared to potassium titanate nanoribbons (30.255 nm). This suggested a much larger projected surface area for MXene within the scanned area. This might be due to the inherent roughness of multi-layered MXene sheets compared to the smoother surface of individual few-layered KTNR nanoribbons. MXene (108.56 nm) also had a higher Sq (root mean square roughness) value compared to the KTNRs (42.233 nm). This confirmed that the MXene surface exhibited more significant height variations, indicating a
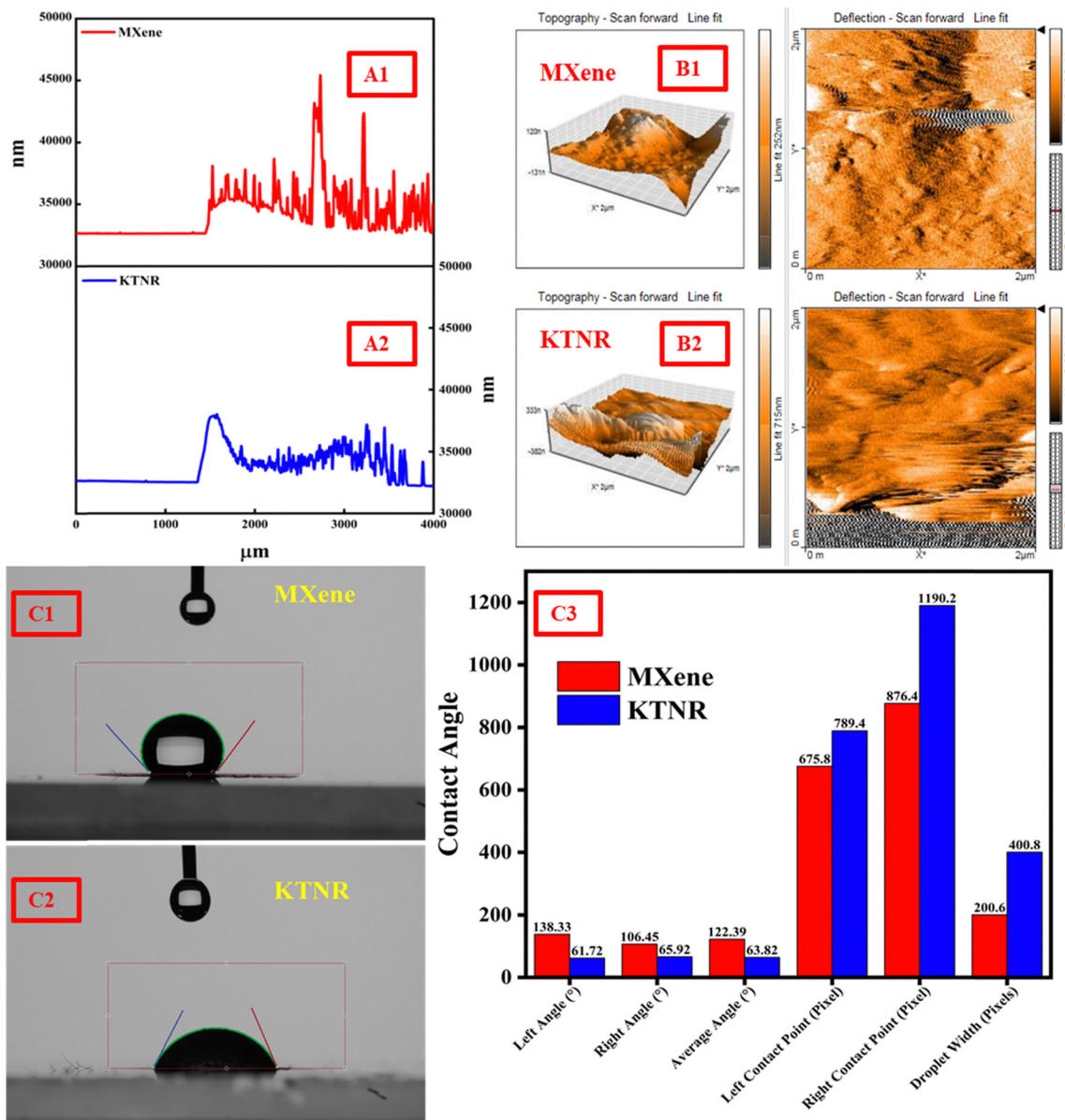
Fig. 4 Surface optical profilometry of (A1) MXene and (A2) KTNRs; AFM (3D) plot to show roughness characteristics and topography for (B1) MXene and (B2) KTNRs; contact angle of 0.1 M phosphate buffer on the surface of the (C1) MXene and (C2) KTNR fabricated GCE; (C3) bar graph comparing parameters for contact angle analysis.

rougher topography. A much higher Sy (skewness) value for MXene (1057.6 nm) was compared to the KTNRs (332.57 nm). Both values were positive, suggesting surfaces with more frequent peaks than valleys. However, the significantly higher value for MXene indicated a much stronger tendency towards a peak-dominated surface profile. MXene (436.12 nm) also had a higher Sp (peak area fraction) value compared to potassium titanate nanoribbons (181.4 nm). This aligned with the other parameters and suggested that the MXene surface has a larger portion covered by peaks compared to valleys. Both Sv (valley area fraction) values were negative, which might be an artifact as discussed previously. However, the absolute value of Sv was much higher for potassium titanate nanoribbons (−151.17 nm) compared to MXene (−621.52 nm). It might also suggest that a

slightly higher portion of the scanned area for the potassium titanate nanoribbons was covered by valleys compared to MXene. The Sm (mean height) values were negative, indicating that the surfaces were lower than the reference plane on average. However, the MXene surface has a slightly more negative Sm value (−10.028 pm) compared to potassium titanate nanoribbons (−10.015 pm). The AFM data suggested a clear difference in surface topography between MXene and potassium titanate nanoribbons. MXene exhibited a significantly rougher surface with larger height variations, a stronger tendency for peaks, and a larger portion of the surface covered by peaks. In contrast, the potassium titanate nanoribbons appeared to have a smoother surface with less pronounced height variations and a more balanced distribution of peaks

and valleys (considering the uncertainty with Sv). The rougher surface of MXene, characterized by its higher Sa, Sq, Sy, and Sp values, could potentially offer a higher surface area for improved performance in electrochemical sensor applications. This increased surface area can provide more active sites for analyte molecules to adsorb, leading to potentially higher sensitivity. However, considering thin film formation, the higher surface roughness of the MXene film suggested a potentially larger effective surface area for applications like catalysis or electrochemical sensing. However, it might also hinder electron transport in electronic devices. The flatter and smoother potassium titanate nanoribbon film might offer less surface area but could potentially allow for more efficient electron transfer across the electrode surface. Further analysis and testing are necessary to determine how these surface properties translate to sensor performance for specific applications.

The provided Fig. 4(C1 and C2) presented the contact angles measured between a drop of 0.1 M phosphate buffer electrolyte and the surface of the MXene and KTNR fabricated GCE. The average contact angle for MXene (122.39°) indicated a hydrophobic surface whereas the average contact angle of KTNR (63.82°) suggested a hydrophilic surface. Generally, a moderately hydrophilic surface was preferred for electrochemical sensors. This allows for good wettability by the electrolyte solution while maintaining some degree of control over the adsorption/desorption processes of analyte molecules at the electrode surface. A low contact angle like that of KTNRs indicates good wettability, meaning the electrolyte can easily penetrate the electrode pores and reach the active material. This is essential for efficient ion transport and redox reactions. Proper wetting ensures good contact between the electrolyte

and the electrode surface, facilitating fast charge transfer and improving the overall kinetics of the electrochemical process. Highly hydrophobic surfaces can hinder electrolyte interaction and limit sensor performance. Highly hydrophilic surfaces might allow for excessive non-specific adsorption of molecules from the electrolyte, leading to background noise and decreased sensor sensitivity.[50] Based on the contact angle data, KTNRs with a more hydrophilic surface (average angle of 63.82°) appeared to be a better candidate for an electrochemical sensor compared to MXene (average angle of 122.39°). A bar graph is provided to represent the parameters owing to the calculation of contact angle (Fig. 4(C3)). The surface roughness could influence the effective contact angle. Rougher surfaces could exhibit higher contact angles even for hydrophilic materials like MXene in this case. The specific target analyte and the desired electrochemical process could also play a role in determining the optimal surface wettability. Other factors like surface chemistry and charge distribution could also influence the interaction between the electrode surface and the analyte/electrolyte. While the contact angle data suggested that KTNRs might be more favourable due to their hydrophilicity, further testing with the target analyte and optimization of the electrode surface properties would be necessary to achieve the best performance for a specific electrochemical sensing application.

3.6. Material characterizations and electrochemical techniques

3.6.1. Stability study for MAX phase, MXene, and KTNR fabricated GCEs. An experiment was performed to compare the stability of MAX phase, MXene and KTNR electrodes for 5 mM $K_3[Fe(CN)_6]$ oxidation in 0.1 M KCl solution over multiple CV cycles (10 and 100 cycles) (Fig. 5(A1 and A2), (B1 and B2) and
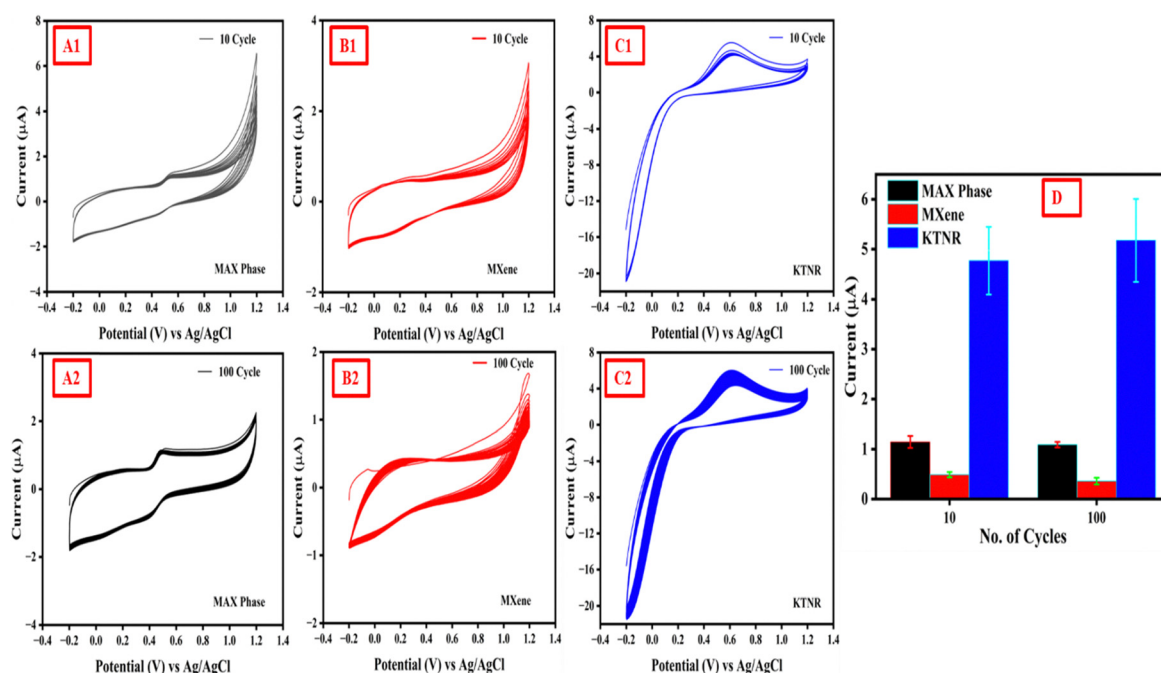

Fig. 5 Stability study of (A1) and (A2) MAX phase/GCE, (B1) and (B2) MXene/GCE and KTNRs and (C1) and (C2) employing 10–200 cycles in 5 mM $K_3[Fe(CN)_6]$; (D) error bar graph showing peak currents against 10 and 100 cycles for MAX phase, MXene and KTNRs.

(C1 and C2)).[51] The current values and their standard deviations were provided for each electrode at different cycle numbers. All electrodes fabricated with MAX phase, MXene, and KTNRs showed a decreasing trend in current with increasing cycle number. For MAX phase, MXene, and KTNRs, the current value starts at 1.27 µA, 5.44 µA, and 5.51 µA in 10 cycles and decreases to 1.15 µA, 4.24 µA and 4.37 µA at 100 cycles. This suggests a loss of electrocatalytic activity for the KTNRs over time. The MAX phase and MXene fabricated electrodes showed a huge drop in current with consecutive cycles, but the change in current at the oxidation peak is less pronounced when compared to KTNRs, which showed a broad error bar. The standard deviations for both electrodes are relatively small compared to the current values, indicating good reproducibility of the measurements. The alternate increase and decrease in current density suggested a loss of electrocatalytic activity over time, which could be due to several factors. The MAX phase, MXene or KTNR nanostructures could be degrading during the cycling process, which could be due to the electrochemical breakdown of the materials or the dissolution of metal ions from the electrode.[52] The surface of the electrodes could be fouled by reaction products or other impurities in the electrolyte.[53] This would block the active sites on the electrode and hinder electron transfer. Lastly, the electrode–electrolyte interface could be weakened over time. This would lead to an increase in resistance and a decrease in current density. The stability of KTNRs can be compared to the MXene and MAX phase by comparing the decrease in current density for both materials over the same number of cycles. A smaller decrease in current density for the KTNRs indicated better stability. However, if the anodic peak currents of KTNRs and MXene are to be compared, the KTNRs show much more significant current 4–5 folds greater than that of MXene and MAX phase fabricated electrodes over multiple cycles (Fig. 5(D)). The cathodic current represents the reduction process. The cathodic current was observed to be higher for KTNRs in both the 10-cycle and 100-cycle tests. The potential range for all three materials was similar, suggesting that the differences in current are not due to a wider electrochemical window for the KTNRs. The possibilities, owing to large cathodic current, might be related to the KTNRs, being nanoribbons, likely possessing a higher surface area compared to the MXene and MAX phase fabricated GCE. A larger surface area is ought to provide more active sites for electrochemical reactions, leading to increased current. The potassium ions in the KTNRs may interact with the redox species $(Fe(CN)_6^{3-})$ in the electrolyte, leading to a synergistic effect that enhances the reduction process. The unique structure of the KTNRs might have facilitated faster charge transfer during the reduction process, which could be due to efficient ion diffusion within the nanoribbons or other factors related to their crystal structure. Hence, the KTNRs exhibited better electrochemical stability, especially over multiple cycles. This would mean that the material could maintain the active sites and charge transfer capabilities, resulting in sustained high cathodic current even after repeated cycling.[54,55] Also the broad window of MAX phase and MXene suggested them to be energy storage materials, while KTNRs exhibit a much better catalytic property as an electrode material.

3.6.2. Understanding the properties of electrode materials using various electrochemical techniques. The intricate properties of all electrode materials were subjected to electrochemical techniques such as CV, DPV, and EIS in 5 mM $K_3[Fe(CN)_6]$ containing 0.1 M KCl. The electrocatalytic properties of the KTNRs, MXene, and MAX phase were studied through CV and DPV. The CV and DPV voltammograms suggest that the KTNR-fabricated GCE exhibited the highest electron transfer compared to MXene and MAX phase fabricated GCEs. The CV graph (Fig. 6(A)) was observed to have a sharp peak of KTNRs having an I_{pa} almost 4 times the anodic peak current (I_{pa} = 3.96 µA), which demonstrated faster reaction kinetics, while the MXene and MAX phase having I_{pa} = 0.69 µA and 0.38 µA, respectively, had much broader peaks, indicating a slower reaction. It was also confirmed by DPV (Fig. 6(B)) where a high peak current in the KTNR (I_{pa} = 1.15 µA) curve was observed compared to MXene (I_{pa} = 0.98 µA) and MAX phase (I_{pa} = 0.46 µA) indicating greater electrode activity for the redox reaction of $K_3[Fe(CN)_6]$. A more positive peak potential for KTNRs (E_{pv} = 0.39 V) signified a lower overpotential, meaning that the electrode requires less or optimal energy to drive the reduction reaction compared to MXene (E_{pv} = 0.43 V) and MAX phase (E_{pv} = 0.16).[56] The effective surface area by KTNRs, MXene and MAX phase fabricated electrodes were calculated to be 3.47×10^{-8} cm^2 s^{-1}, 1.054×10^{-9} cm^2 s^{-1} and 3.196×10^{-10} cm^2 s^{-1}, respectively. By considering all parameters, the MXene and MAX phase as electrode materials ought to be better as energy storage materials, while the KTNRs showed better electro-catalytic performance.

The EIS Nyquist plots for the KTNR fabricated GCE show a lower impedance compared to its precursors MXene and MAX phase. This indicates that the KTNR electrode has a higher ability to transfer charge at the electrode–electrolyte interface. In other words, it has better electrocatalytic activity.[57] In the Nyquist plot, the imaginary impedance (Z'') is plotted on the y-axis and the real impedance (Z') is plotted on the x-axis (Fig. 6(C)). The equivalent circuit model simplified KTNR electrode–electrolyte interface and the fitting method used was Randomize + Simplex while the parameters were the values of the components in the equivalent circuit $(R_1 + Q_1/(R_2 + C_2/(R_3 + C_3/(R_4 + W_4)))) + C_5/R_5$ that best match the experimental EIS data. The R_1 = 2.028 Ω or the solution resistance (R_s) represented the resistance of the electrolyte solution between the working and reference electrodes. A lower R_s suggests a more conductive electrolyte solution. The R_2 = 195 Ω and R_3 = 938.9 Ω referred to charge transfer resistance (R_{ct}) that represented the resistance to electron transfer between the electrode and the electrolyte. The Nyquist plot showed a smaller semicircle diameter at low frequencies indicating a lower R_{ct} and faster charge transfer kinetics.[58] In the image, the KTNR electrode has a smaller semicircle diameter compared to the MXene and MAX phase. The diameter of the semicircle for KTNRs extends less towards the lower frequencies, and it could also indicate faster mass transfer for the KTNR electrode. The value of R_4 = 23 601 Ω suggested a Warburg impedance W_4 = 0.2033 × 10^{-9} Ohm s$^{-1/2}$ implying the resistance to mass transfer of ions
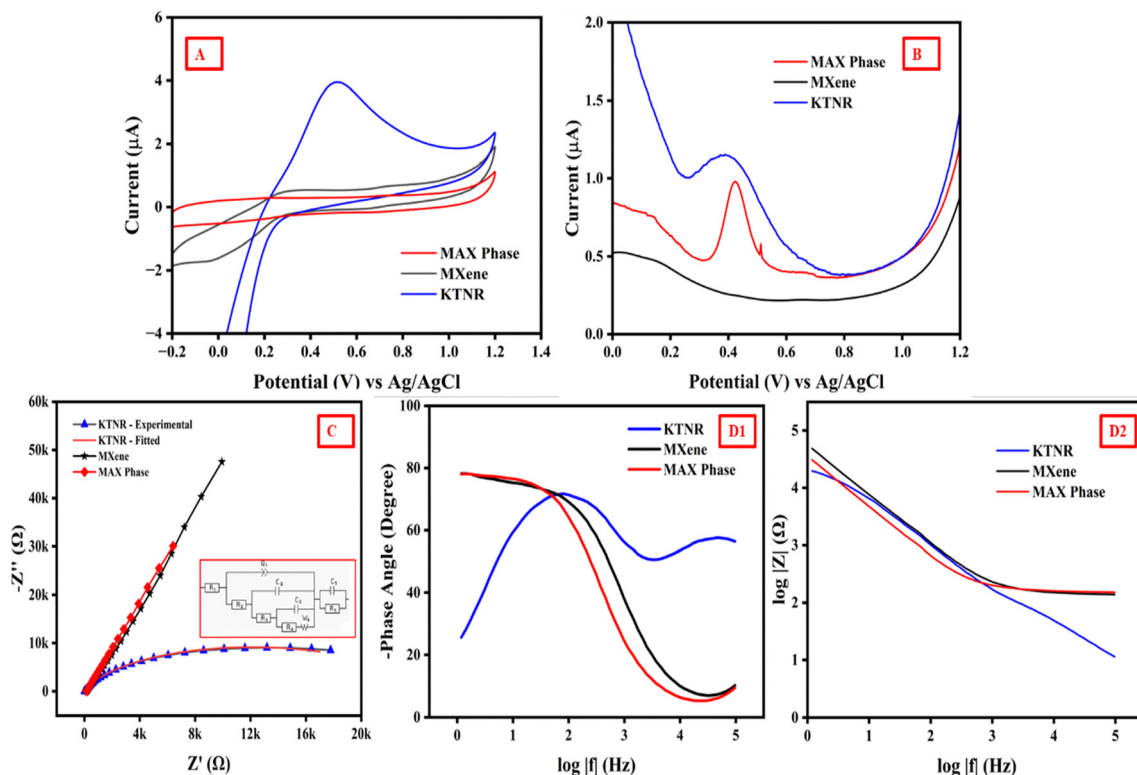
Fig. 6 (A) CV, (B) DPV, (C) EIS Nyquist plots (inset: equivalent circuit) and (D) Bode plot for the KTNR, MXene and MAX phase fabricated GCE in 5 mM $K_3[Fe(CN)_6]$ in 0.1 M KCl electrolyte.

within the electrolyte, which in-turn was related to the rate of the reaction at the electrode surface.[59] The possible film resistance $R_5 = 271\,304\ \Omega$ represented the resistance of the Nafion-stabilized KTNR thin film formed on the electrode surface. The $C_2 = 0.509 \times 10^{-6}$ F or the double layer capacitance represented the capacitance between the electrode–electrolyte interface. The $C_3 = 0.2197\ \mu F$ and $C_5 = 1.287 \times 10^{24}$ F represented capacitance associated with the Nafion stabilized film on the electrode surface or porosity of KTNRs as electrode materials.[60] Lastly, the constant phase element ($Q_1 = 4.239 \times 10^{-6}$ F s^{a-1}) was an element that could be used to model a more complex capacitance where the parameter "$a1 = 0.7535$" determined the deviation from ideal capacitance behaviour of the equivalent circuit. The exchange current density represents the rate of electron transfer at equilibrium, where the forward and reverse reaction rates are equal.

It's a fundamental parameter that reflects the intrinsic activity of the electrode material. The key relationship is derived from the Butler–Volmer equation, and under conditions of small overpotential (near equilibrium), it simplifies to $I_0 = RT/(nFR_{ct})$; where I_0 = exchange current density (A cm^{-2}), R = ideal gas constant (8.314 J mol^{-1} K^{-1}), T = absolute temperature (K), n = number of electrons transferred in the redox reaction, F = Faraday constant (96 485 C mol^{-1}) and R_{ct} = charge-transfer resistance (Ω). The R_{ct} values in this case were calculated to be 938.9 Ω, 230 346 Ω and 326 328 Ω for KTNRs, MXene and MAX phase, respectively, which yielded the corresponding I_0 values of 2.75×10^{-5} A cm^{-2}, 1.22×10^{-7} A cm^{-2} and 7.92×10^{-8} A cm^{-2}. The exchange current density

showed that KTNR/GCE has much better intrinsic electrocatalytic activity.[61]

A Bode plot (Fig. 6(D1 and D2)) typically shows two key features for EIS data, one being the phase angle which indicates the phase shift between the applied voltage and the resulting current and the second is impedance magnitude ($\log|Z|$) which represents the overall resistance to current flow in the system. At high frequencies, the phase angle typically approaches towards 0 degrees, indicating minimal phase shift. As the frequency decreases, the phase angle becomes more negative, reflecting the increasing influence of capacitive behaviour. At even lower frequencies, the phase angle might approach −90 degrees for a purely capacitive response. At high frequencies, the impedance magnitude was usually dominated by solution resistance and shows a plateau in the $\log|Z|$ *vs.* $\log|f|$ plot. As the frequency decreases, the impedance magnitude might start to increase due to the influence of charge transfer resistance and other processes. The provided information suggested that a complex equivalent circuit model was used to capture the EIS response of the KTNRs, MXene, and MAX phase fabricated GCE.

3.6.3. Mechanism of electro-oxidation of ciprofloxacin on the active working surface area of the KTNR fabricated electrode. Ciprofloxacin is a fluoroquinolone antibiotic known for its broad-spectrum activity. It is a zwitterionic molecule, meaning that it can exist with both positive and negative charges depending on the pH. KTNRs are a metal oxide material having surface charge, which can influence the interaction with ciprofloxacin molecules.

The process of electrochemical oxidation involved the transfer of electrons from ciprofloxacin molecules to the electrode surface, resulting in the oxidation of ciprofloxacin. The steps involved were diffusion, adsorption, electron transfer, desorption and diffusion, which can be observed in Fig. 7(C). Ciprofloxacin molecules in the bulk solution diffuse towards the surface of the potassium titanate electrode. Ciprofloxacin molecules could interact with the electrode surface through various forces like electrostatic interactions, hydrogen bonding, or van der Waals forces. The net charge of ciprofloxacin at pH 8 (likely negatively charged) and the surface charge of the KTNRs (which could also be pH-dependent) would influence this adsorption process. At the electrode surface, ciprofloxacin molecules lose electrons to the electrode, undergoing oxidation. The specific mechanism of electron transfer could involve direct interaction with the electrode or the participation of intermediate species formed on the electrode surface. The oxidized ciprofloxacin molecules desorbed from the electrode surface and get diffused back into the bulk solution. The factors that could affect the process are pH, electrode potential and scan rate. The pH of the solution could influence the net charge of ciprofloxacin and the surface charge of the KTNR electrode.

An optimal pH might exist for balancing the electrostatic interactions and promoting efficient electron transfer. The applied potential at the electrode can influence the rate of electron transfer. A higher positive potential might be required to drive the oxidation reaction. In cyclic voltammetry experiments, the scan rate can affect the observed current response. At faster scan rates, the diffusion process might become limiting, leading to a deviation from the ideal behaviour. The electrochemical oxidation of ciprofloxacin at a potassium titanate electrode ought to be a complex process involving mass transport (diffusion), surface interaction (adsorption/desorption), and electron transfer. The efficiency of this process depends on various factors, like pH, electrode potential, and surface properties, which were studied and optimized in the later part of the research.

3.6.4. Optimization of pH for ciprofloxacin detection using the KTNR/GCE. Ciprofloxacin is a zwitterionic molecule, meaning it can exist with both positive and negative charges depending on the pH. At lower pH (around 4), ciprofloxacin is likely mostly protonated (positively charged) due to the acidic environment. As observed in Fig. 7(A1 and A2), when the pH increases from 4 to 11, the solution becomes more basic, and ciprofloxacin loses its
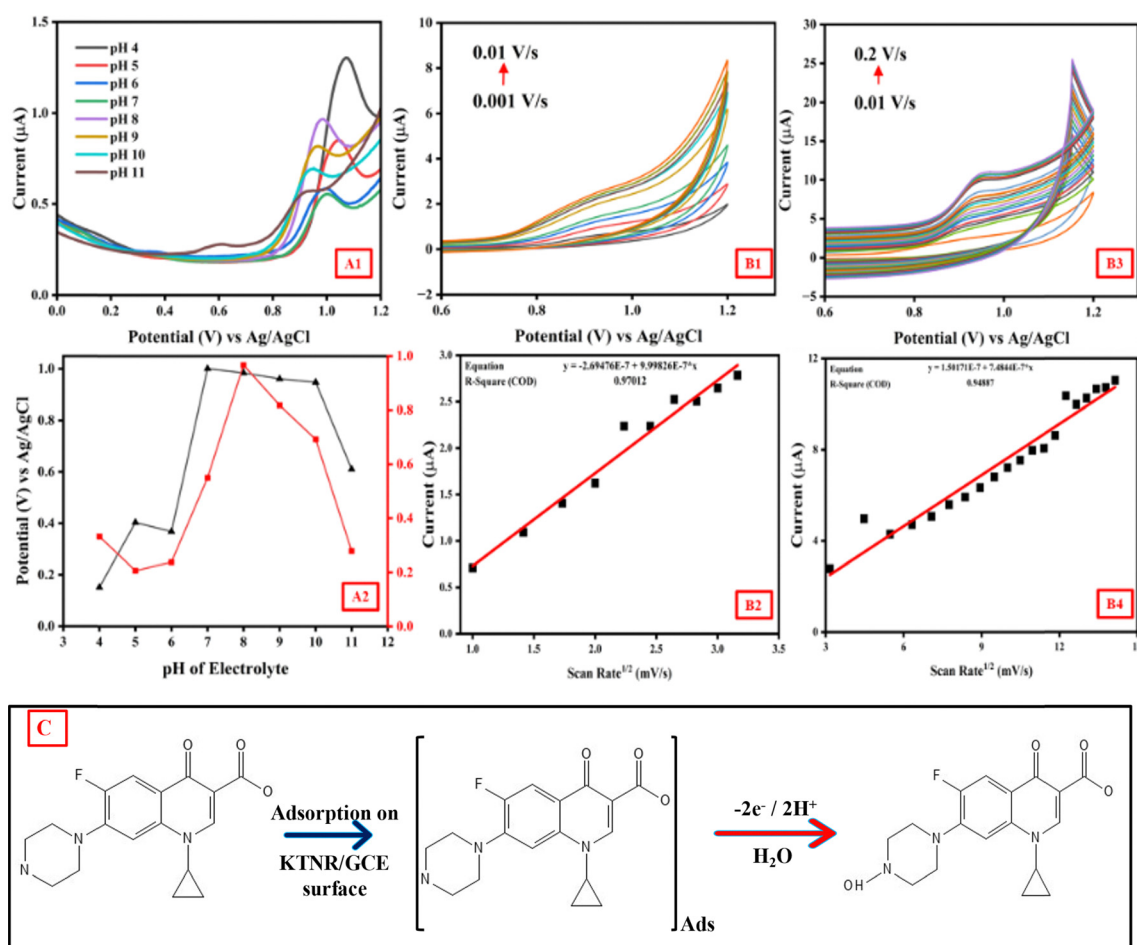

Fig. 7 (A1) Study of pH to optimize the voltammetric detection of ciprofloxacin using KTNR/GCE, (A2) line + scatter plot to show the correlation of peak potential (E_{pv}) and anodic peak current (I_{pa}) vs. pH of the 0.1 M phosphate buffer electrolyte containing ciprofloxacin; study of different scan rate CV (B1) 0.01–0.01 mV s^{-1} and (B3) 0.01–0.2 mV s^{-1} in 0.1 M phosphate buffer at optimized pH = 8 and, their corresponding regression plots (B2) and (B4); (C) illustration of the mechanism of electro-oxidation of ciprofloxacin at the active surface area of the KTNR/GCE.

protons, becoming increasingly deprotonated (negatively charged). To deal with surface charge interaction, KTNRs are a metal oxide material that also exhibit a surface charge depending on the pH. At lower pH, the KTNR active surface might be positively charged. As the pH increased, the surface charge of the KTNRs could become more negative. When the pH was low (acidic), both ciprofloxacin (positively charged) and the KTNR surface (positively charged) experienced electrostatic repulsion. This repulsion could hinder the adsorption of ciprofloxacin molecules onto the electrode surface and slow down the electron transfer process. As the pH increased, ciprofloxacin became increasingly deprotonated (negatively charged). This could lead to attractive forces between the negatively charged ciprofloxacin and the potentially negatively charged KTNR surface at higher pH. This attraction could enhance the adsorption of ciprofloxacin molecules and potentially promote the electron transfer process, leading to a higher current at a slightly less positive potential (anodic shift). The observed optimal pH of 8 might be a balance between these two effects. At pH 8, ciprofloxacin might be sufficiently deprotonated to favour adsorption on the electrode surface while minimizing any repulsion from the electrode surface itself. Since the pH 8 is between the reference pK_a values (pK_{a1} = 5.17 and pK_{a2} = 8.74), ciprofloxacin will likely exist in a zwitterionic form in the 0.1 M pH 8 phosphate buffer. The carboxylic acid group (pK_{a1}) will likely be deprotonated (negatively charged) as the solution's pH is higher than its pK_a. The primary amine group (pK_{a2}) might be partially protonated (positively charged) due to the pH being slightly lower than its pK_{a2}. This could lead to the most efficient electron transfer and the highest anodic peak current for ciprofloxacin oxidation. The anodic peak shifted towards more positive potentials with increasing pH suggesting a change in the rate of the electro-oxidation reaction. The shift likely reflected a slower reaction rate at lower pH (due to electrostatic repulsion) and a potentially faster rate at higher pH (due to enhanced adsorption). Ciprofloxacin might undergo multiple redox reactions involving different electron transfers and protonations. This complex mechanism could lead to non-linear behavior, as the relative contributions of these reactions can vary with pH. Ciprofloxacin, like many drugs, exists in different protonation states depending on the pH of the solution.[62] These different protonation states could also have varying redox potentials, which might have led to non-linearity.[63] The nature of the electrode surface, including its composition and roughness, can influence the adsorption of ciprofloxacin and its redox behavior since the fabrication of an electrode using the drop-casting method might always lead to handling errors.[64–66] The ionic strength of the solution could also influence the activity coefficients of the species involved in the redox reaction, leading to deviations from the expected linear relationship.[67–69] Temperature could also be a parameter that might have influenced the kinetics of the redox reaction and the stability of the redox species.[70,71] This can further complicate the relationship between redox potential and pH.

3.6.5. Impact of scan rates on ciprofloxacin detection using KTNR/GCE. The CV curves showed anodic peaks around 0.8 V

to 1.0 V at pH 8, which corresponded to the oxidation of ciprofloxacin. As the scan rate increased (from 1 mV s^{-1} to 200 mV s^{-1}), the following trends were observed (Fig. 7(B1 and B3)). The anodic peak current increased and the peak potential (where the current is maximum) shifted slightly towards more positive potentials. The linear regression plots of anodic current (I_p) vs. square root of scan rate ($v^{1/2}$) for three scan rate ranges (1–10 mV s^{-1}, 10–100 mV s^{-1}, and 100–200 mV s^{-1}) suggested a diffusion-controlled electrochemical process for ciprofloxacin oxidation at least for the lower scan rates (1–10 mV s^{-1}). The high R-squared values 0.97012 and 0.94887 for the linear plots $I_p = 9.99826 \times 10^{-7} \times v^{1/2} + 2.69476 \times 10^{-7}$ (Fig. 7(B2)) and $I_p = 7.4844 - 7 \times v^{1/2} + 1.50171 \times 10^{-7}$ (Fig. 7(B4)), respectively, which indicated good linear relationships between the I_p vs. $v^{1/2}$ in these two lower scan rate ranges. The deviation from linearity observed at higher scan rates (above 10 mV s^{-1}) might be due to limitations in the diffusion process of ciprofloxacin molecules towards the electrode surface at faster scan rates. The regression suggested a diffusion-controlled process. The number of electrons transferred (n) was 1 for ciprofloxacin oxidation and the concentration (C) of analyte was 90 μM. The electrode surface area (A) was calculated to be 0.071 cm^2 for the GCE. The diffusion coefficient (D) was calculated using the Randles–Sevcik equation, with the formula: $I_p = (2.69 \times 10^5) \times n^{3/2} \times C \times A \times D^{1/2} \times v^{1/2}$. The calculated average diffusion coefficient of 2.21×10^{-11} cm^2 s^{-1} was well consistent within a reasonable range for ciprofloxacin in phosphate buffer electrolyte. Diffusion-controlled reactions: at slower scan rates, diffusion processes can become limiting, leading to a more reversible behaviour. As the scan rate increases, the system may not have enough time for the diffusion of reactants and products, leading to a deviation from reversibility and a crossover of the anodic and cathodic peaks.

The crossing of the CV curves at higher potentials in the 10 mV s^{-1} to 200 mV s^{-1} scan rate range suggested a change in the electrochemical behaviour of the system (Fig. 7(B3)). If the charge transfer kinetics were slow, increasing the scan rate could lead to a shift in the peak potentials and a crossover of the curves. At higher scan rates (>50 mV s^{-1}), the capacitive current associated with double-layer charging became more significant.[72] This could contribute to the observed crossover, as the capacitive current can mask the faradaic current associated with the redox processes. At higher potentials beyond 1 V, the electrode surface might undergo oxidation or reduction processes that affected the electrochemical behaviour.[73,74] These changes could also lead to a shift in the peak potentials and a crossover of the curves.[75,76] PB electrolyte containing ciprofloxacin could have caused a potential drop (IR drop) across the electrolyte hemisphere, which might have distorted the CV curves, especially at higher scan rates. This IR drop could lead to a shift in the peak potentials and a crossover of the curves.[77]

Based on the observed behaviour, a possible mechanism for ciprofloxacin oxidation at the KTNR/GCE could be proposed. Ciprofloxacin molecules in the bulk solution diffused towards the electrode surface. At the electrode surface, ciprofloxacin underwent an electron transfer reaction, getting oxidized.

The oxidized ciprofloxacin got desorbed from the electrode surface and diffused back into the bulk solution. At slower scan rates, where the diffusion process was dominant, the current increased as the scan rate increases since there was more time for ciprofloxacin molecules to diffuse towards the electrode surface and get oxidized. At faster scan rates, the diffusion process might become limited. The ciprofloxacin molecules might not be able to reach the electrode surface fast enough to keep up with the electron transfer reaction rate. This could lead to a deviation from the ideal linear relationship between the current and the square root of scan rate. The CV data suggested that the oxidation of ciprofloxacin at the KTNR/GCE was an electrochemically active process. The slight shift in the anodic peak potential with increasing scan rate might be due to kinetic limitations or a combination of diffusion and kinetic control at higher scan rates.

3.6.6. Electrochemical sensing studies of ciprofloxacin using the KTNR/GCE. CV aimed to investigate the electrochemical response of ciprofloxacin at a KTNR/GCE in a linear concentration range of 0.6 μM to 147.2 μM (Fig. 8(A1)). The CV likely showed indistinguishable but linearly increasing

oxidation peaks at a specific potential, indicating the electrochemical oxidation of ciprofloxacin at the KTNR/GCE. The position of this peak could be determined at beyond 1.0 V as observed in the voltammogram. It was also observed that the oxidation peak current (I_{pa}) increased as the concentration of ciprofloxacin (C) in the electrolyte solution increased. Although no clear peaks were formed, the voltammogram suggested that KTNR was actively involved in catalysis, which indicated that more ciprofloxacin molecules were being oxidized at the electrode with higher concentrations. Ideally, the plot of peak current *vs.* ciprofloxacin concentration exhibited a linear relationship having an equation $I_{pa} = 1.86503 \times 10^{-8} \times C + 9.36571 \times 10^{-7}$ with an $R^2 = 0.94776$ (Fig. 8(A2)) within a specific concentration range of 0.6 μM to 147.2 μM. The LOD was calculated to be 0.07 μM and LOQ was 0.213 μM. The sensitivity of the KTNR/GCE for ciprofloxacin sensing through CV was 0.282 μA μM^{-1} cm^{-2}.

DPV was used, which is a more sensitive technique compared to CV for quantitative analysis. The potential range scanned was from 0.6 V to 1.2 V (Fig. 8(B1)). The DPV plot showed a well-defined peak at a specific potential, corresponding to the oxidation of ciprofloxacin at the KTNR electrode. The $E_{pv} = 0.98$ was

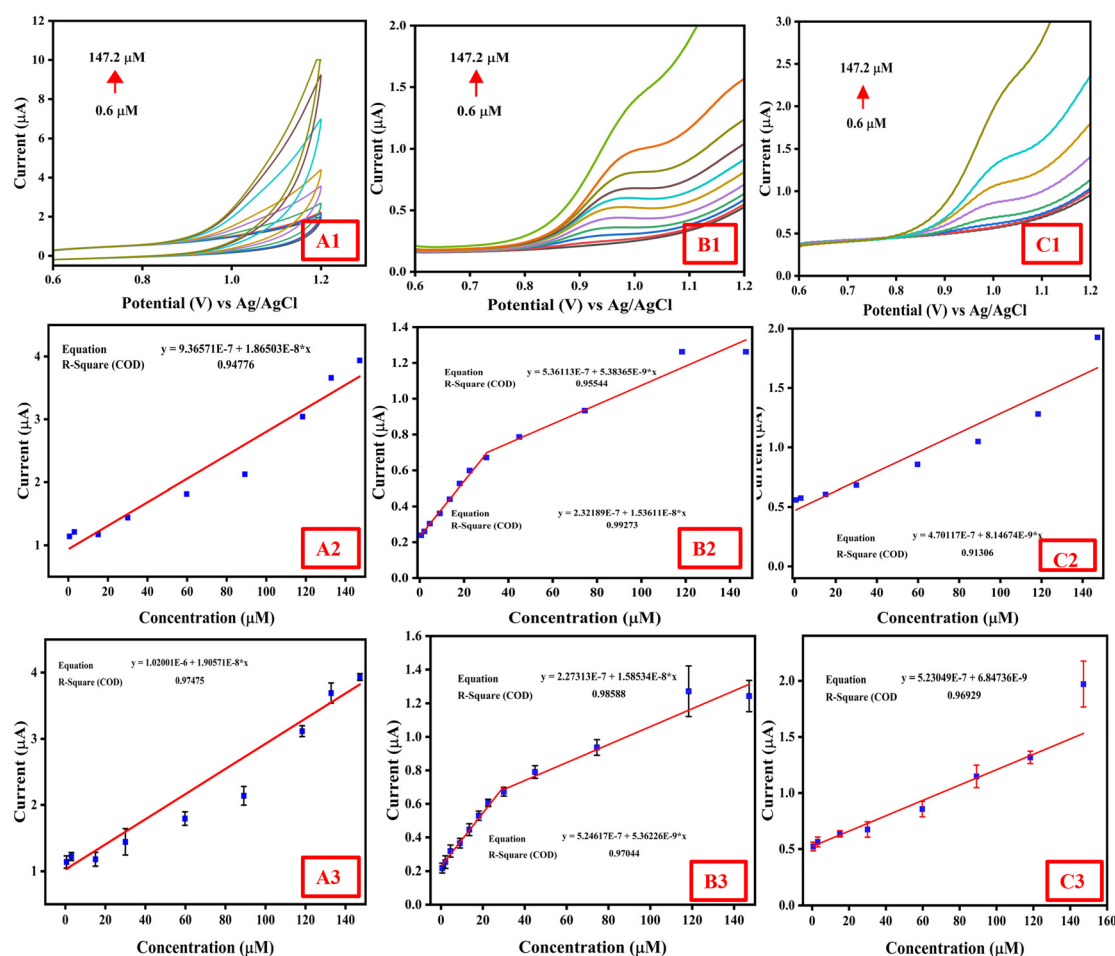**Fig. 8** (A1) and (A2) CV response and corresponding regression plot; (B1) and (B2) DPV response and corresponding regression plot; (C1) and (C2) SWV response and corresponding regression plot of KTNRs to obtain the linear concentration range of ciprofloxacin in 0.1 M phosphate buffer pH = 8; triplicate data on (A3) CV, (B3) DPV and (C3) SWV response curves with regression plots showing excellent replicability.

the peak voltage that could be determined from the voltammogram. The image showed that the peak current for the ciprofloxacin oxidation peak increases with the concentration of ciprofloxacin in the electrolyte solution. One could analyze the linearity by plotting the peak current data points for different concentrations and fitting a straight line through them $I_{pa} = 1.53611 \times 10^{-8} \times C + 2.32189 \times 10^{-7}$ and $I_{pa} = 5.38365 \times 10^{-9} \times C + 5.36113 \times 10^{-7}$ (Fig. 8(B2)). The respective R^2 value of the fit, *i.e.*, 0.99273 and 0.9554, indicated how excellent the data corresponded to a linear relationship. Through DPV, the KTNR/GCE offered a sensitivity of 0.0986 µA µM^{-1} cm^{-2}, while having an LOD and LOQ of 0.0608 µM and 0.184 µM, respectively.

SWV being a variant of pulse voltammetry was employed to confirm linearity observed in DPV. It also offers advantages like higher sensitivity and lower background current compared to CV. Each curve in the plot likely corresponded to the SWV response for a different concentration of ciprofloxacin in the electrolyte solution, which also relayed to the oxidation at the KTNR active electrode surface (Fig. 8(C1)). The equation $I_{pa} = 8.14674 \times 10^{-9} \times C + 4.70117 \times 10^{-8}$ with an R^2 value = 0.91306, shows its consistency with DPV results (Fig. 8(C2)). Also, the LOD and LOQ were calculated, which were found to be 0.0264 µM and 0.08 µM, respectively, while offering a sensitivity of 0.113 µA µM^{-1} cm^{-2}. The replicability showed consistent replicability in data of CV, DPV and DPV, as shown in Fig. 8(A3, B3 and C3).

Overall, considering the highest sensitivity value and lowest LOD. The DPV data suggested that the KTNR/GCE electrode was a more promising tool for the quantitative detection of ciprofloxacin within a certain concentration range of 0.6 µM to 147.2 µM over CV and SWV. DPV and SWV minimize the contribution of the charging current by measuring the current at specific points after the potential step. This led to a sharper and more well-defined peak compared to CV. The current measured with DPV and SWV was constant throughout the experiment, which reflected the faradaic current at specific points in the potential waveform. This resulted in a more prominent current response compared to the smooth regular curve observed in CV. The observed increase in oxidation peak current with increasing concentration indicated a linear relationship that could be exploited for analytical purposes. This dynamic range of micromolar concentration can be

used for quantitative analysis of ciprofloxacin concentration in unknown samples using the KTNR/GCE electrode. A comparison with previous reported non-enzymatic electrochemical sensors for ciprofloxacin detection is tabulated in Table 2.

3.6.7. Reproducibility of KTNR/GCE for ultrasensitive detection of ciprofloxacin. Ten freshly fabricated KTNR electrodes were tested through CV, DPV and SWV (Fig. 9(A1, B1, and C1)) in the same laboratory conditions and room temperature (25 °C) to check the reproducibility of the electrodes towards ciprofloxacin detection using the CV technique at a random concentration. The system's viability was confirmed by an error bar graph (Fig. 9(A2, B2 and C2)) that practically demonstrates the stability of the electrode. The peak currents averaged at 0.91 µA ± 0.15%, 0.484 µA ± 0.19% and 1.2 µA ± 0.12% were obtained from CV, DPV and SWV. The results showed excellent reproducibility owing to the novelty of the newly developed KTNR-based electrochemical sensor. The variation estimated as RSD values of 0.15%, 0.19% and 0.12% was calculated, which could be owing to the handling error and manual fabrication of the electrodes. However, if the sensor fabrication samples were not stored properly after preparation, the electrode materials of the sensor could be prone to oxidation and the performance might degrade.

3.6.8. Selectivity of the KTNR/GCE and effect of interfering compounds against ciprofloxacin detection. To ensure selective healthcare monitoring, the KTNR-modified GCE was expected to present a high selectivity for ciprofloxacin against other antibiotics and drugs administered to humans and animals, especially poultry and cattle. To confirm the selectivity of the sensor, the CV was obtained in solutions containing 10 µM of ciprofloxacin (CIP) against the same concentration of other antibiotics like enrofloxacin (EF), enrofloxacin (NOR), ofloxacin (OFL) and, diclofenac (DCF) (Fig. 10(A)). In addition to ciprofloxacin detection, the selectivity of KTNR/GCE was investigated using separate 0.1 M phosphate buffer pH = 8 containing ciprofloxacin, norfloxacin, ofloxacin and diclofenac individually. The adsorption capacity and selectivity of the KTNR/GCE for other drug analytes were almost three folds lower compared to ciprofloxacin, which showed the highest peak current at a particular 0.98 V potential window, indicating that the binding selectivity of KTNRs was specific to the ciprofloxacin molecules.

Table 2 Reported literature on non-enzymatic electrochemical sensors for the detection of ciprofloxacin

| Materials/electrode	Method	Linear range (µM)	LOD (µM)	Real samples	Ref.
Co-MOFs/PLA	DPV	0.5–150	0.017	Drug	78
GO/SPCE	DPV	1–8	0.3	Milk	79
TiO$_2$/PVA/GCE	DPV	10–120	0.04	Rain water	80
f-MWCNTs/PANI/GCE	LSV	0.1–1, 1–20	0.08	Pharmaceuticals	81
f-MWCNT-coated GCE	SWV	5–100	0.16	Hospital effluent, wastewater, natural water	82
BaCuSi$_4$O$_{10}$/GCE	DPV	0.05–150	0.0009	Pharmaceuticals	83
Pt-RGO/GCE	DPV	10–25	1.53	Tap water, river water	84
CRGO/GCE	SWV	6–60	0.5	Pharmaceuticals, milk	85
Ch-AuMIP/GCE	DPV	1–100	0.21	Tap water, milk, mineral water, pharmaceuticals	86
BiPO$_4$/GO-MMIPs/PGE	SWSV	39–740	0.4	Blood serum, milk	87
Fe-g-C$_3$N$_4$/PGE	DPV	0.001–1	0.0054	Blood serum	88
ChCl/CPE	SWV	0.005–200	0.00036	CIP eye drops, eggs, river water	89
KTNR/GCE	CV, DPV, SWV	0.6–147.2	0.07, 0.0608, 0.0264	Honey, milk, eggs, marine water, Ganga water, organic fertilizer, soil, Simulated body fluid	This work
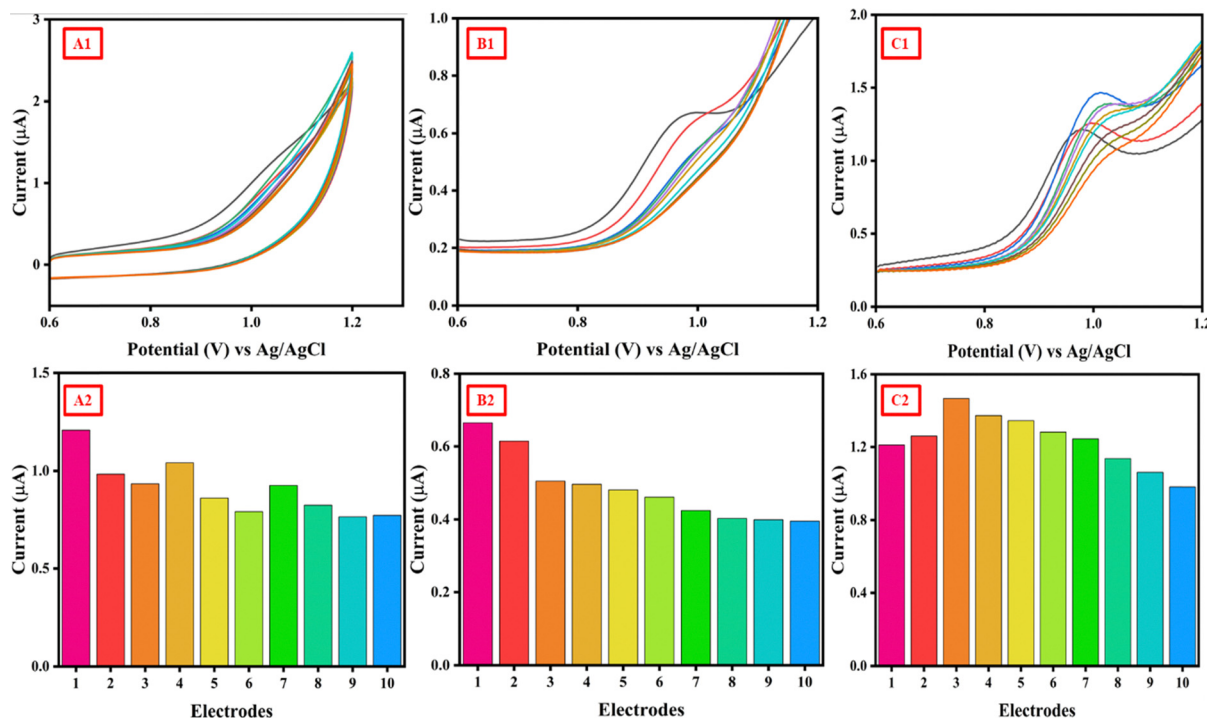
Fig. 9 Reproducibility of KTNR-fabricated GCEs based on CV (A1) and (A2), DPV (B1) and (B2) and SWV (C1) and (C2) towards efficient sensing of ciprofloxacin.

The high selectivity can be explained by the unique morphology and high catalytic properties of the KTNRs. However, the sensor is not at par selective for ciprofloxacin when it was compared with enrofloxacin which showed twice the amount of current signal within the same potential window. Therefore, this result has provided evidence that KTNR/GCE was selective to other antibiotic classes and drugs but not enrofloxacin due to its similar nature to ciprofloxacin oxidation. Both are zwitterionic molecules that exhibit similar results when tested.

The effect of common inorganic ions, compounds and, drugs existing in various real matrices where ciprofloxacin is detected were also investigated through CV. Compounds like dopamine (DP), uric acid (UA), urea (UR), ascorbic acid (AA), glucose (G), and ions, such as Ca^{2+}, Na^+, K^+, Mg^{2+} and HCO_3^- were chosen to test while their concentrations were a hundred times higher than that of ciprofloxacin, $i.e.$, by adding 1000 μM of interfering compounds/ions and 10 μM ciprofloxacin in 0.1 M phosphate buffer pH = 8, and the results are shown in

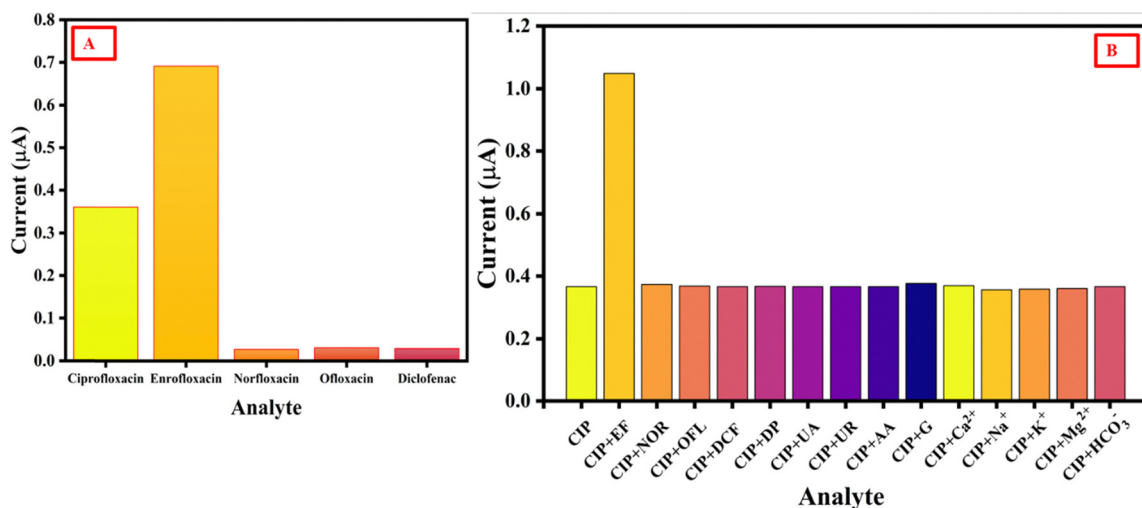**Fig. 10** (A) Selectivity of the KTNR/GCE for ciprofloxacin (CIP) against enrofloxacin (EF), norfloxacin (NOR), ofloxacin (OFL), and diclofenac (DCF); (B) interference test for electrochemical ciprofloxacin (CIP), a determination under the influence of other co-existing compounds like dopamine (DP), uric acid (UA), urea (UR), ascorbic acid (AA), glucose (G), and ions such as Ca^{2+}, Na^+, K^+, Mg^{2+}, and HCO_3^-.

Table 3 Electrochemical trace detection of ciprofloxacin spiked in milk, honey and egg, Ganga water, marine water, soil and organic fertilizer samples using the KTNR-modified electrochemical sensor

Samples	Spiked (μM)	Detected (μM)	Variance	STD	RSD (%)	Recovery (%)
Milk	0	0	0	0	0	0
	15	6.02	40.3202	6.349819	60.41693	40.13333
Honey	0	0	0	0	0	0
	15	15.3	0.045	0.212132	1.400211	102
Egg	0	0	0	0	0	0
	15	14.6	0.08	0.282843	1.911099	97.33333
Marine water	0	0	0	0	0	0
	15	6.56	35.6168	5.967981	55.36161	43.73333
Ganga water	0	0	0	0	0	0
	15	18.6	6.48	2.545584	15.15229	124
Organic fertilizer	0	0	0	0	0	0
	15	11.4	6.48	2.545584	19.28473	76
Soil	0	0	0	0	0	0
	15	8.3	22.445	4.737615	40.66623	55.33333
SBF	0	0	0	0	0	0
	15	15.1	0.005	0.070711	0.469838	100.6667

Fig. 10(B). Also to check the effects of the co-existence of other drugs in real matrices, enrofloxacin, norfloxacin, ofloxacin and diclofenac were taken into consideration in the same manner by checking with 10 μM concentration along with 10 μM ciprofloxacin. The only exception that occurred is in the case of enrofloxacin where the interference could be seen to be quite high.[40] Other than that, the response of the sensor towards bare 10 μM ciprofloxacin solution is quite similar to that toward the mixture of ciprofloxacin and interfering drugs, compounds and ions, suggesting a very excellent anti-interfering ability of KTNR/GCE even in the micro-environment where the amount of interference may be remarkably higher than that of ciprofloxacin. The DPV results indicate that the present interfering substances have negligible or no influence on the ciprofloxacin detection in real matrices other than enrofloxacin being present in them. This also shows that the sensor has excellent recognition ability toward ciprofloxacin detection owing to the unique properties of the KTNRs.

3.6.9. Validation of KTNR/GCE for ciprofloxacin detection in complex matrices. The ultrasensitive detection of trace ciprofloxacin in complex matrices existing in animals, the environment and humans was achieved by the standard addition method. The results are tabulated in Table 3. The developed KTNR-based ciprofloxacin sensor was successful in detecting the trace analyte concentrations in the tested complex matrices of real samples. Recoveries ranging between 40.13% to 124% are practically viable analytical results for a potential electrochemical sensing device. Spiked samples of milk and Ganga water showed low recovery rate indicating the possibility of some interfering compounds being adsorbed or there may be an incident of electro-polymerization of pollutants that causes fouling at the electrode surface which in-turn is hindering the current flow. However, honey, egg and most importantly simulated body fluid (SBF) show excellent recovery rate, indicating the efficacy of the proposed sensing device.

4. Conclusion

In conclusion, this research demonstrated the successful synthesis, characterization and fabrication of a novel 2D MXene-derived potassium titanate nanoribbon-based electrochemical sensor for the ultrasensitive detection of ciprofloxacin. The sensor exhibited exemplary performance in all electrochemical voltammetric techniques (CV, DPV, and SWV) achieving a remarkably low LOD and LOQ while being highly selective for other antibiotics and interfering species except enrofloxacin at the particular pH 8. Notably, the sensor demonstrated practical reliability in complex matrices mainly in egg, honey, and SBF, making it a promising candidate for real-world applications in on-site food safety, environmental monitoring, and healthcare diagnostics. Further studies could focus on optimizing sensor stability and exploring miniaturization techniques for technology readiness level (TLR) upgradation and on-site detection to combat antimicrobial resistance against ciprofloxacin, thus contributing to One Health and Sustainable Development Goals.

Data availability

The data will be made available on request.

Conflicts of interest

There are no conflicts to declare.

References

1 M. LeBel, Ciprofloxacin: Chemistry, Mechanism of Action, Resistance, Antimicrobial Spectrum, Pharmacokinetics,

Clinical Trials, and Adverse Reactions, *Pharmacotherapy*, 1988, **8**, 3–30.

2 D. J. Mason, E. G. M. Power, H. Talsania, I. Phillips and V. A. Gant, Antibacterial action of ciprofloxacin, *Antimicrob. Agents Chemother.*, 1995, **39**, 2752–2758.

3 C. J. Thomson, The global epidemiology of resistance to ciprofloxacin and the changing nature of antibiotic resistance: a 10 year perspective, *J. Antimicrob. Chemother.*, 1999, **43**, 31–40.

4 B. Fantin, *et al.*, Ciprofloxacin dosage and emergence of resistance in human commensal bacteria, *J. Infect. Dis.*, 2009, **200**, 390.

5 C. Herald, *et al.*, Ciprofloxacin induces apoptosis and inhibits proliferation of human colorectal carcinoma cells, *Br. J. Cancer*, 2002, **86**, 443–448.

6 P. M. Peltzer, *et al.*, Ecotoxicity of veterinary enrofloxacin and ciprofloxacin antibiotics on anuran amphibian larvae, *Environ. Toxicol. Pharmacol.*, 2017, **51**, 114–123.

7 A. Hayes, *et al.*, Predicting selection for antimicrobial resistance in UK wastewater and aquatic environments: Ciprofloxacin poses a significant risk, *Environ. Int.*, 2022, **169**, 107488.

8 B. Á. Pataki, *et al.*, Understanding and predicting ciprofloxacin minimum inhibitory concentration in Escherichia coli with machine learning, *Sci. Rep.*, 2020, **10**, 1–9.

9 T. M. J. Ewoldt, *et al.*, Barriers and facilitators for therapeutic drug monitoring of beta-lactams and ciprofloxacin in the ICU: a nationwide cross-sectional study, *BMC Infect. Dis.*, 2022, **22**(1), 611.

10 C. J. Murray, *et al.*, Global burden of bacterial antimicrobial resistance in 2019: a systematic analysis, *Lancet*, 2022, **399**, 629–655.

11 K. C. Mofolorunsho, H. O. Ocheni, R. F. Aminu, C. A. Omatola and O. O. Olowonibi, Prevalence and antimicrobial susceptibility of extended-spectrum beta lactamases-producing Escherichia coli and Klebsiella pneumoniae isolated in selected hospitals of Anyigba, Nigeria, *Afr. Health Sci.*, 2021, **21**, 505–512.

12 L. J. M. Githinji, M. K. Musey and R. O. Ankumah, Evaluation of the fate of ciprofloxacin and amoxicillin in domestic wastewater, *Water, Air, Soil Pollut.*, 2011, **219**, 191–201.

13 H. Liu, *et al.*, The application of UV/O3 process on ciprofloxacin wastewater containing high salinity: Performance and its degradation mechanism, *Chemosphere*, 2021, **276**, 130220.

14 C. H. Johansson, L. Janmar and T. Backhaus, Toxicity of ciprofloxacin and sulfamethoxazole to marine periphytic algae and bacteria, *Aquat. Toxicol.*, 2014, **156**, 248–258.

15 C. C. de Souza, G. F. Alves, T. P. Lisboa, M. A. C. Matos and R. C. Matos, Low-cost paper-based electrochemical sensor for the detection of ciprofloxacin in honey and milk samples, *J. Food Compos. Anal.*, 2022, **112**, 104700.

16 A. Onken, *et al.*, Predominance of multidrug-resistant Salmonella Typhi genotype 4.3.1 with low-level ciprofloxacin resistance in Zanzibar, *PLoS Neglected Trop. Dis.*, 2024, **18**, e0012132.

17 B. Wu, *et al.*, Facile synthesis of dendritic-like CeO_2/rGO composite and application for detection of uric acid and tryptophan simultaneously, *J. Solid State Chem.*, 2021, **296**, 122023.

18 S. Zhang, P. Ling, Y. Chen, J. Liu and C. Yang, 2D/2D porous Co_3O_4/rGO nanosheets act as an electrochemical sensor for voltammetric tryptophan detection, *Diamond Relat. Mater.*, 2023, **135**, 109811.

19 A. P. Roy, *et al.*, Development of MWCNT/Gd_2O_3/SnO_2 composite fabricated GCE for voltammetric detection of L-cysteine, *J. Surf. Interfac.*, 2024, **16**, 100267.

20 A. P. Roy, *et al.*, Emerging trends on nanomaterial-based simultaneous electrochemical sensing of dopamine and acetaminophen, *Results Chem.*, 2024, **7**, 101489.

21 G. Li, *et al.*, Highly stable electrochemical sensing platform for the selective determination of pefloxacin in food samples based on a molecularly imprinted-polymer-coated gold nanoparticle/black phosphorus nanocomposite, *Food Chem.*, 2024, **436**, 137753.

22 L. Xie, *et al.*, An efficient voltammetric sensing platform for trace determination of Norfloxacin based on nanoplate-like α-zirconium phosphate/carboxylated multiwalled carbon nanotube nanocomposites, *Microchem. J.*, 2024, **206**, 111451.

23 X. Wan, *et al.*, UiO-66/Carboxylated Multiwalled Carbon Nanotube Composites for Highly Efficient and Stable Voltammetric Sensors for Gatifloxacin, *ACS Appl. Nano Mater.*, 2023, **6**, 19403–19413.

24 G. Li, *et al.*, Lamellar α-Zirconium Phosphate Nanoparticles Supported on N-Doped Graphene Nanosheets as Electrocatalysts for the Detection of Levofloxacin, *ACS Appl. Nano Mater.*, 2023, **6**, 17040–17052.

25 G. Li, *et al.*, Molecularly imprinted polypyrrole film-coated poly(3,4-ethylenedioxythiophene):polystyrene sulfonate-functionalized black phosphorene for the selective and robust detection of norfloxacin, *Mater. Today Chem.*, 2022, **26**, 101043.

26 T. Mathai, T. Pal, N. Prakash and S. Mukherji, Portable biosensor for the detection of Enrofloxacin and Ciprofloxacin antibiotic residues in food, body fluids, environmental and wastewater samples, *Biosens. Bioelectron.*, 2023, **237**, 115478.

27 Z. U. D. Babar, *et al.*, MXenes in healthcare: synthesis, fundamentals and applications, *Chem. Soc. Rev.*, 2025, DOI: **10.1039/d3cs01024d**.

28 A. Appu Mini and V. Raghavan, Mxene-derived $Na_2O_7Ti_3$ nanoribbon as a promising electrode material for the detection of ethyl paraoxon in complex matrices, *Microchem. J.*, 2024, **201**, 110674.

29 Y. Dong, *et al.*, Ti_3C_2 MXene-Derived Sodium/Potassium Titanate Nanoribbons for High-Performance Sodium/Potassium Ion Batteries with Enhanced Capacities, *ACS Nano*, 2017, **11**, 4792–4800.

30 F. Zheng, F. Ma, L. Cai and X. Zhang, Proton conduction enabled highly selective acetonitrile detection at moderate operating temperature by using Ag-decorated sodium titanate nanoribbons, *J. Mol. Liq.*, 2024, **395**, 123843.

31 D. C. B. Alves, *et al.*, Hydrogen sensing in titanate nanotubes associated with modulation in protonic conduction, *Nanotechnology*, 2011, **22**(23), 235501.

32 Y. Zhang, *et al.*, Excessive use of enrofloxacin leads to growth inhibition of juvenile giant freshwater prawn Macrobrachium rosenbergii, *Ecotoxicol. Environ. Saf.*, 2019, **169**, 344–352.

33 L. Cai and X. Zhang, Sodium titanate: A proton conduction material for ppb-level NO_2 detection with near-zero power consumption, *J. Hazard. Mater.*, 2024, **462**, 132781.

34 C. Mestres, M. A. Alsina, M. A. Busquets, I. Haro and F. Reig, Interaction of Enrofloxacin with Phospholipid Mono-and Bilayers, *Langmuir*, 1994, **10**, 767–772.

35 W. Liu, *et al.*, Inhibition of microbial growth on air cathodes of single chamber microbial fuel cells by incorporating enrofloxacin into the catalyst layer, *Biosens. Bioelectron.*, 2015, **72**, 44–50.

36 A. Windust, *et al.*, High polarity analytes in food - enrofloxacin and sulfadiazine in bovine tissue (CCQM-K141), *Metrologia*, 2019, **56**, 08005.

37 Gaussian 09 Citation|Gaussian.com, **https://Gaussian.com/g09citation**.

38 M. P. Thukkaram, *et al.*, Titanium carbide MXene and V_2O_5 composite-based electrochemical sensor for detection of bisphenol A, *Microchem. J.*, 2023, **193**, 109004.

39 A. A. Mini, *et al.*, CuO nanoparticles passivated 2D MXene-based voltammetric sensor for detecting environmental hazardous pollutant, *Microchem. J.*, 2024, **201**, 110648.

40 A. Chakravorty and V. Raghavan, Proton conductive 2D MXene-derived potassium titanate nanoribbons fabricated electrochemical platform for trace detection of enrofloxacin, *Chemosphere*, 2024, **366**, 143520.

41 S. Wang, *et al.*, Molten salt synthesis of MXene-derived hierarchical titanate for effective strontium removal, *J. Hazard. Mater.*, 2024, **469**, 134079.

42 Y. Dong, *et al.*, Ti_3C_2 MXene-Derived Sodium/Potassium Titanate Nanoribbons for High-Performance Sodium/Potassium Ion Batteries with Enhanced Capacities, *ACS Nano*, 2017, **11**, 4792–4800.

43 S. Awasthi, S. K. Pandey, J. K. Gaur and C. Srivastava, Load-bearing study and interfacial interactions of hydroxyapatite composite coatings for bone tissue engineering, *Mater. Chem. Front.*, 2022, **6**, 3731–3747.

44 S. Awasthi, J. K. Gaur, S. K. Pandey, M. S. Bobji and C. Srivastava, High-Strength, Strongly Bonded Nanocomposite Hydrogels for Cartilage Repair, *ACS Appl. Mater. Interfaces*, 2021, **13**, 24505–24523.

45 K. Singh, *et al.*, Interpretation of Adsorption Behavior of Carboxymethyl Cellulose onto Functionalized Accurel Polymeric Surface, *Ind. Eng. Chem. Res.*, 2020, **59**, 19102–19116.

46 S. K. Pandey, Novel and Polynuclear K- And Na-Based Super-alkali Hydroxides as Superbases Better Than Li-Related Species and Their Enhanced Properties: An Ab Initio Exploration, *ACS Omega*, 2021, **6**, 31077–31092.

47 N. Lele, M. F. Bambo, E. M. Mmutlane and L. N. Dlamini, Construction of a multifunctional MXene@β-cyclodextrin nanocomposite with photocatalytic properties, *Emergent Mater.*, 2023, **6**, 605–626.

48 M. Catti, I. Pinus and A. Scherillo, On the crystal energy and structure of A_2TinO_{2n+1} (A = Li, Na, K) titanates by DFT calculations and neutron diffraction, *J. Solid State Chem.*, 2013, **205**, 64–70.

49 B. Anasori, M. R. Lukatskaya and Y. Gogotsi, 2D metal carbides and nitrides (MXenes) for energy storage, *Nat. Rev. Mater.*, 2017, **2**, 1–17.

50 L. Li, *et al.*, Surface and Interface Engineering of Nanoarrays toward Advanced Electrodes and Electrochemical Energy Storage Devices, *Adv. Mater.*, 2021, **33**, 2004959.

51 S. A. Zargar, *et al.*, Synthesis of novel 2D/2D $Ti_3C_2T_x$ MXene/1T-MoS_2 heterostructure enhanced with carbon nanotubes as a highly-efficient electrode for hybrid capacitive deionization, *J. Alloys Compd.*, 2024, **981**, 173765.

52 D. Wang, Z. Zhu, B. He, Y. Ge and D. Zhu, Effect of the breakdown time of a passive film on the electrochemical machining of rotating cylindrical electrode in $NaNO_3$ solution, *J. Mater. Process. Technol.*, 2017, **239**, 251–257.

53 W. Sun, *et al.*, Cathodic membrane–based electrochemical redox process for water treatment: a review, *Curr. Opin. Chem. Eng.*, 2024, **44**, 101023.

54 Y. Sun, S. Gao, F. Lei and Y. Xie, Atomically-thin two-dimensional sheets for understanding active sites in catalysis, *Chem. Soc. Rev.*, 2015, **44**, 623–636.

55 P. Jiang, *et al.*, A Cost-Effective 3D Hydrogen Evolution Cathode with High Catalytic Activity: FeP Nanowire Array as the Active Phase, *Angew. Chem.*, 2014, **126**, 13069–13073.

56 C. Costentin, M. Robert and J. M. Savéant, Catalysis of the electrochemical reduction of carbon dioxide, *Chem. Soc. Rev.*, 2013, **42**, 2423–2436.

57 R. Tatara, *et al.*, The Effect of Electrode-Electrolyte Interface on the Electrochemical Impedance Spectra for Positive Electrode in Li-Ion Battery, *J. Electrochem. Soc.*, 2019, **166**, A5090–A5098.

58 H. N. Tsao, *et al.*, Influence of the interfacial charge-transfer resistance at the counter electrode in dye-sensitized solar cells employing cobalt redox shuttles, *Energy Environ. Sci.*, 2011, **4**, 4921–4924.

59 H. Watanabe, Y. Sugiura, I. Shitanda and M. Itagaki, Faradaic impedance and discharge reactions in lithium sulfur battery with sparingly solvating electrolyte, *Electrochim. Acta*, 2024, **477**, 143759.

60 S. D. Sutar, I. Patil, H. Parse, P. Mukherjee and A. Swami, $Ti_3C_2T_x$/TiO_2@GO* Heterostructure: A Strategy to Design High-Specific Capacitive Electrodes for a Solid-State Supercapacitor, *ACS Appl. Energy Mater.*, 2024, **7**(10), 4353–4364.

61 H. Ibrahim and Y. Temerk, Surface decoration of functionalized carbon black nanoparticles with nanosized gold particles for electrochemical sensing of diuretic spironolactone in patient plasma, *Microchem. J.*, 2022, **178**, 107425.

62 J. Sun, *et al.*, Determination of lipophilicity of two quinolone antibacterials, ciprofloxacin and grepafloxacin, in the protonation equilibrium, *Eur. J. Pharm. Biopharm.*, 2002, **54**, 51–58.

63 P. M. Becker, K. Heinze, B. Sarkar and J. Kästner, Redox-Acid/Base Phase Diagrams as an Entry to Computational Redox Chemistry, *ChemElectroChem*, 2024, **11**, e202400301.

64 M. Elancheziyan, M. Singh and K. Won, Gold Nanoparticle-Embedded Thiol-Functionalized $Ti_3C_2T_x$ MXene for

Sensitive Electrochemical Sensing of Ciprofloxacin, *Nano-materials*, 2024, **14**, 1655.

65 C. Bhuvaneswari and S. Ganesh Babu, Review of 2-D support-based nanocomposites for electrocatalytic detection of pharmaceutical drugs, *J. Mater. Sci.*, 2024, **59**(26), 11687–11717.

66 D. Tonelli, I. Gualandi, E. Scavetta and F. Mariani, Focus Review on Nanomaterial-Based Electrochemical Sensing of Glucose for Health Applications, *Nanomaterials*, 2023, **13**, 1883.

67 J. Blumberger, L. Bernasconi, I. Tavernelli, R. Vuilleumier and M. Sprik, Electronic Structure and Solvation of Copper and Silver Ions: A Theoretical Picture of a Model Aqueous Redox Reaction, *J. Am. Chem. Soc.*, 2004, **126**, 3928–3938.

68 H. Tamura, Theorization on ion-exchange equilibria: activity of species in 2-D phases, *J. Colloid Interface Sci.*, 2004, **279**, 1–22.

69 M. H. de Sá and C. M. Pereira, The relevance of the initial conditions in glassy carbon electrode sensing applications: the ferri/ferrocyanide redox reaction model system in aqueous solution, *Electrochim. Acta*, 2024, **489**, 144158.

70 Z. Yu, *et al.*, Electrolyte engineering for efficient and stable vanadium redox flow batteries, *Energy Storage Mater.*, 2024, **69**, 103404.

71 J. Pati and R. S. Dhaka, Mixed polyanionic $NaFe_{1.6}V_{0.4}(PO_4)(SO_4)_2$@CNT cathode for sodium-ion batteries: Electrochemical diffusion kinetics and distribution of relaxation time analysis at different temperatures, *J. Power Sources*, 2024, **609**, 234646.

72 P. Zhu and Y. Zhao, Effects of electrochemical reaction and surface morphology on electroactive surface area of porous copper manufactured by Lost Carbonate Sintering, *RSC Adv.*, 2017, **7**, 26392–26400.

73 R. Gómez and J. Clavilier, Electrochemical behaviour of platinum surfaces containing (110) sites and the problem of the third oxidation peak, *J. Electroanal. Chem.*, 1993, **354**, 189–208.

74 M. Grdeń, M. Łukaszewski, G. Jerkiewicz and A. Czerwiński, Electrochemical behaviour of palladium electrode: Oxidation, electrodissolution and ionic adsorption, *Electrochim. Acta*, 2008, **53**, 7583–7598.

75 D. O. Wipf, E. W. Kristensen, M. R. Deakin and R. M. Wightman, Fast-Scan Cyclic Voltammetry as a Method to Measure Rapid, Heterogeneous Electron-Transfer Kinetics, *Anal. Chem.*, 1988, **60**, 306–310.

76 Y. Ruiz, *et al.*, Repeatability of low scan rate cyclic voltammetry in bioelectrochemical systems and effects on their performance, *J. Chem. Technol. Biotechnol.*, 2020, **95**, 1533–1541.

77 S. Anantharaj and S. Noda, iR drop correction in electrocatalysis: everything one needs to know!, *J. Mater. Chem. A*, 2022, **10**, 9348–9354.

78 M. Yahyapour, M. Ranjbar and A. Mohadesi, Determination of ciprofloxacin drug with molecularly imprinted polymer/co-metal organic framework nanofiber on modified glassy carbon electrode (GCE), *J. Mater. Sci.: Mater. Electron.*, 2021, **32**, 3180–3190.

79 M. Pan, P. Guo, H. Liu, J. Lu and Q. Xie, Graphene oxide modified screen-printed electrode for highly sensitive and selective electrochemical detection of ciprofloxacin residues in milk, *J. Anal. Sci. Technol.*, 2021, **12**, 1–7.

80 J. Zhao, P. Huang and W. Jin, Electrochemical sensor based on TiO_2/polyvinyl alcohol nanocomposite for detection of ciprofloxacin in rainwater, *Int. J. Electrochem. Sci.*, 2021, **16**, 211018.

81 P. Jain and R. V. Motghare, Electro-Oxidation and Determination of Ciprofloxacin at f-MWCNT@Poly-Aniline Glassy Carbon Electrode, *J. Electrochem. Soc.*, 2022, **169**, 056515.

82 A. Chaabani, T. Ben Jabrallah and N. Belhadj Tahar, Electrochemical Oxidation of Ciprofloxacin on COOH-Functionalized Multi-Walled Carbon Nanotube–Coated Vitreous Carbon Electrode, *Electrocatalysis*, 2022, **13**, 402–413.

83 G. Muungani, V. Moodley and W. E. van Zyl, Solid-state synthesis of the phyllosilicate Effenbergerite ($BaCuSi_4O_{10}$) for electrochemical sensing of ciprofloxacin antibiotic in pharmaceutical drug formulation, *J. Appl. Electrochem.*, 2022, **52**, 285–297.

84 T. S. H. Pham, *et al.*, Graphene Nanocomposites Based Electrochemical Sensing Platform for Simultaneous Detection of Multi-drugs, *Electroanalysis*, 2022, **34**, 435–444.

85 L. V. Faria, *et al.*, Square-Wave Voltammetry Determination of Ciprofloxacin in Pharmaceutical Formulations and Milk Using a Reduced Graphene Oxide Sensor, *J. Braz. Chem. Soc.*, 2019, **30**, 1947–1954.

86 S. G. Surya, *et al.*, A chitosan gold nanoparticles molecularly imprinted polymer based ciprofloxacin sensor, *RSC Adv.*, 2020, **10**, 12823–12832.

87 S. Kumar, P. Karfa, K. C. Majhi and R. Madhuri, Photocatalytic, fluorescent BiPO4@Graphene oxide based magnetic molecularly imprinted polymer for detection, removal and degradation of ciprofloxacin, *Mater. Sci. Eng., C*, 2020, **111**, 110777.

88 H. S. Vedhavathi, B. P. Sanjay, M. Basavaraju, B. S. Madhukar and N. Kumara Swamy, Development of ciprofloxacin sensor using iron-doped graphitic carbon nitride as transducer matrix: Analysis of ciprofloxacin in blood samples, *J. Electrochem. Sci. Eng.*, 2022, **12**, 59–70.

89 W. D. Adane, B. S. Chandravanshi and M. Tessema, A simple, ultrasensitive and cost-effective electrochemical sensor for the determination of ciprofloxacin in various types of samples, *Sens. Bio-Sens. Res*, 2023, **39**, 100547.